QUANTUM CHEMICAL STUDIES OF THE METAL ION SOLVATION AND COORDINATION AND ELUCIDATION OF THE ISOBUTYLENE POLYMERIZATION

by

Minh Nguyen Vo

B.S. in Chemical Engineering, Bucknell University, 2014

Submitted to the Graduate Faculty of

Swanson School of Engineering in partial fulfillment

of the requirements for the degree of

Master of Science

University of Pittsburgh

2017

UNIVERSITY OF PITTSBURGH

SWANSON SCHOOL OF ENGINEERING

This thesis was presented

by

Minh Nguyen Vo

It was defended on

March 31, 2017

and approved by

J Karl Johnson, Ph.D., W. K. Whiteford Professor,
Department of Chemical & Petroleum Engineering

Peng Liu, Ph.D., Assistant Professor, Department of Chemistry

Thesis Advisor: John A. Keith, Ph.D., Assistant Professor, Department of Chemical & Petroleum Engineering

QUANTUM CHEMICAL STUDIES OF METAL ION SOLVATION AND COORDINATION AND ELUCIDATION OF THE ISOBUTYLENE POLYMERIZATION MECHANISM

Minh Nguyen Vo, M.S.

University of Pittsburgh, 2017

Quantum chemistry calculations using Kohn-Sham density function theory (DFT) are widely used for atomic scale predictions of properties of atoms, molecules, and materials. This thesis will report studies using DFT modeling to 1) understand how to improve the quality of continuum solvation models for predicting solvation free energies and the coordination of metal ions, 2) how to accurately model adjacent lanthanide metal separations, and 3) provide insight into the atomic scale isobutylene polymerization mechanism. This thesis will show current performance and existing challenges when using DFT modeling for these applications.

TABLE OF CONTENTS

LIST OF TABLES

LIST OF FIGURES

PREFACE

First, I would like to thank my thesis advisor, Dr. John Keith, for this patience and guidance. I would also like to thank Dr. J Karl Johnson for his guidance, motivation, and insight. In addition, I would like to acknowledge my committee member, Dr. Peng Liu, for his insightful comments and feedbacks. My sincere thanks also go to Dr. Vyacheslav Bryantsev for the opportunity to intern at the Oak Ridge National Laboratory under his mentorship. I have gained valuable experience working with him.

Last, but not least, I would like to express my profound gratitude to my friends and family for providing me with unfailing support and continuous encouragement.

1.0 INTRODUCTION

Significant progress has been made to the development of advanced molecular theories in recent decades[1,2]. This has promoted the use of quantum chemistry in many different fields including chemistry, biochemistry, and material science. Kohn-Sham density function theory (DFT) methods are widely used for atomic scale prediction of properties of atoms, molecules, and materials[3]. DFT, using functional, allows many-body systems to be conveniently modeled with an electron density. Furthermore, chemical properties in the solvent phase can be predicted using DFT in conjunction with continuum solvation models (CSM). The CSM treats solvent phase as a continuous medium, which drastically reduces the computational expense by omitting the use of explicit solvent molecules.

For many systems, GSMs[4-8] can provide fast and reliable solvation energies for atoms and molecules, but they are known to break down for some systems, specifically for small charged systems. In these systems, CSMs tend to improperly model the strong interaction between the solute molecule and local solvent molecules[9,10]. It has been shown in the literature that adding explicit solvent molecules can improve the accuracy of the CSMs[11,12]. Deciding where and how many solvent molecules should be used can be challenging[13,14]. In Chapter 2, we propose a systematic and automatable computational approach to predict solvation free energies of ionic species.

In 2011, the Department of Energy published a list of critical materials, which are essential for the clean energy economy[15]. Many listed critical and near critical materials are rare earth metals are members of the lanthanide series. Current processes for separating adjacent lanthanides, however, are expensive and inefficient. DFT modeling can facilitate the discovery of new extractants for lanthanide separation, but modeling complexation of heavy elements can be a challenging task as adequate treatment of relativistic effects, and sometimes spin-orbit coupling, is needed[16]. In Chapter 3, we will report the effect of different basis set and levels of theory on selectivity trend across the lanthanide series.

Elucidating catalytic reaction mechanism with quantum modeling is becoming increasing popular in recent years[1]. One of the most important precursors for many commercial polymer products is polyisobutylene. Industrial production of polyisobutylene has existed for over 50 years, but the knowledge of the mechanism reaction is limited. Chapter 4 will discuss the use of DFT to understand the reaction mechanism of polyisobutylene at the molecular level.

2.0 PREDICTING HYDRATION FREE ENERGIES OF METAL IONS

2.1 INTRODUCTION

Accurate solvation energies are essential for calculating condensed phase properties such as redox potentials and pK_as[17], and they play an importance role in the fields of chemistry and biochemistry. Solvation energies are usually computed using an appropriate thermodynamic cycle. One can predict the solvation energies by extensively sample configurations of solvent molecules clustering the solute, but such approaches can be computationally expensive and sometimes difficult to execute without a robust and reliable force field. Alternatively, one can quickly estimate the solvation energy of a solute by using the continuum solvation models[4-8]. These models, however, often yield inaccurate solvation energies for solutes with concentrated charge density. This effect is prominently observed for small ions, where there is strong interaction between the local solvent molecules and the solute molecule[9,10].

The common practice to improve the solvation energy calculations is to introduce explicit solvent molecules in charged systems. Bryantsev and co-workers proposed the mixed cluster/continuum models, which accurately predicted the solvation energies of H^+ and Cu^{2+} with an absolute mean error of 2.0 kcal/mol[18,19]. The approaching is promising, but the approach is hardly reproducible as there is no consensus on how to effectively construct a mixed cluster[13,14].

In this study, we propose a systematic and automatable computational approach to predict the solvation free energies of ionic species. Our approach uses a black box global optimization code, ABCluster[20], to generate micro solvated clusters that are then used in the mixed cluster/continuum models. We progressively increase the number of solvent molecules in the cluster until we observe a convergence in the solvation energies. In addition, our approach is also effective in predicting the complexation coordination of metal ions with chelating agents. In the next section, we will go over the technical approach of our approach.

2.2 COMPUTATIONAL DETAILS AND METHODOLOGY

2.2.1 Metal and water clusters generation

Molecular clusters containing a metal ion with specified number of water molecules were generated using the rigid molecular cluster module in the ABCluster code[20]. We describe water with classical CHARMM forcefield[21] that uses the TIP4P model[22] for water and metal ions treated with a Lennard-Jones potential. ABCluster generated 10,000 structures, and the 100 lowest energy structures were then optimized at the B3LYP[23]/def2-SVP[24] level of theory with the RI-J approximation[25] in Turbomole version 6.6[26]. All calculations were performed with Grimme's D3 dispersion[27]. Frequency calculations were performed at B3LYP/def2-SVP basis set to verify that geometries were the minima and to compute zero point energies and thermal corrections. Single-point energy calculations were performed with def2-TZVP basis set[24]. Solvation effects were approximated with COSMO continuum solvation model[7].

2.2.2 Thermodynamic cycle for computing $\Delta G^*_{solv}(M^{k\pm})$

The Boltzmann weighted average energy of the 100 optimized clusters in gas and solvation phases were used to calculate the solvation energies of metal ion using the thermodynamic cycle in Figure 1.

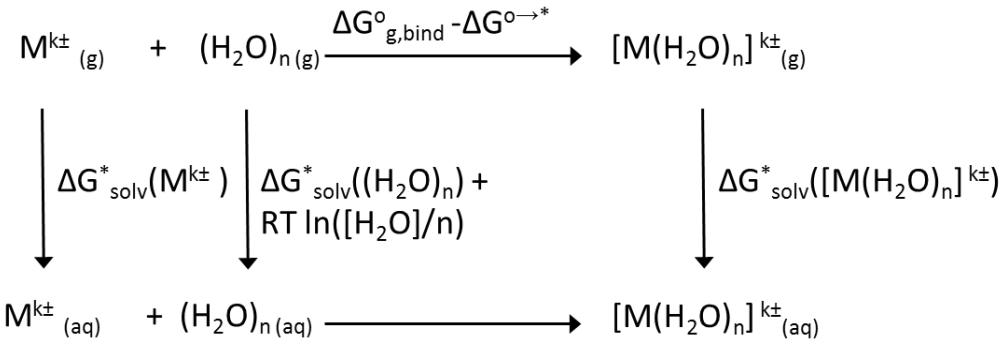

Figure 1. Thermodynamic cycle for the calculation of solvation free energies of ions.

The solvation free energy of an ion, $\Delta G^*_{solv}(A^{m\pm})$ is given as

$$\Delta G^*_{solv}(M^{k\pm}) = \Delta G^o_{g,bind} - \Delta G^{o\rightarrow *} + \Delta G^*_{solv}([M(H_2O)_n]^{k\pm}) - \Delta G^*_{solv}((H_2O)_n) - RT\ln([H_2O]/n) \quad (1)$$

Solvating a solute molecule involves transferring it from the standard state of 1 atm (24.46 L/mol) to the standard state of 1 mol/L (1 M). As the result, an energy correction term is necessary. The standard state correction, $\Delta G^{\circ\rightarrow *}$, represents the change in the free energy of transfer of 1 mol of solute from the gas phase at the standard state of 1 atm to the aqueous phase at a standard state of 1 M.

$$\Delta G^{o\rightarrow *} = -T\Delta S^{o\rightarrow *} = RT\ln(V^\circ/V^*) = RT\ln(24.46) = 1.89 \text{ kcal/mol } (T = 298.15 \text{ K}) \quad (2)$$

Equation 2 is applied to each gas-phase reactant and product results in the correction given in the upper leg of the thermodynamic cycle shown in Figure 1. With water clusters, an additional correction, RT ln([H2O]/n) is needed because the pure solvent $H_2O_{(l)}$ is adopted as the reference state for the solvent in the lower leg of the thermodynamic cycle. This correction represents a free energy change associated with moving a solvent from a standard state solution phase concentration of 1 M to standard state of the pure liquid of 55.34M. Discussion of these free energy corrections can be found in [18].

2.3 RESULTS AND DISCUSSION

2.3.1 Solvation free energy of Cu^{2+} ion

The solvation free energies of Cu^{2+} ion clustered with 6, 10, 18, and 30 explicit water molecules are -409.6, -498.3, -511.8, and -513.8 kcal/mol, respectively. The solvation energy of Cu^{2+} ion clearly improves systematically with increasing numbers of explicit water molecules. This trend is consistent with the trend reported by Bryantsev and co-workers[19], Figure 1. Those clustered Cu^{2+} complexes used to compute $\Delta G_{solv}(Cu^{2+})$ in Bryantsev's work were the lowest-energy structures from their extensive study of the geometric structures of hydrated Cu^{2+} complexes[19]. While these clusters were built through trial and error and with chemical intuition, our structures were generated through an automated process without a priori knowledge. Our calculated $\Delta G_{solv}(Cu^{2+})$ appears to converge at an absolute solvation energy of -513.8 kcal/mol as the calculated $\Delta G_{solv}(Cu^{2+})$ with 30 explicit water molecules is only 2.0 kcal/mol more negative

than the $\Delta G_{solv}(Cu^{2+})$ with 18 explicit water molecules. This leads to a relatively small error of 1.3% compared to the experimental value of 507.0 kcal/mol[28].

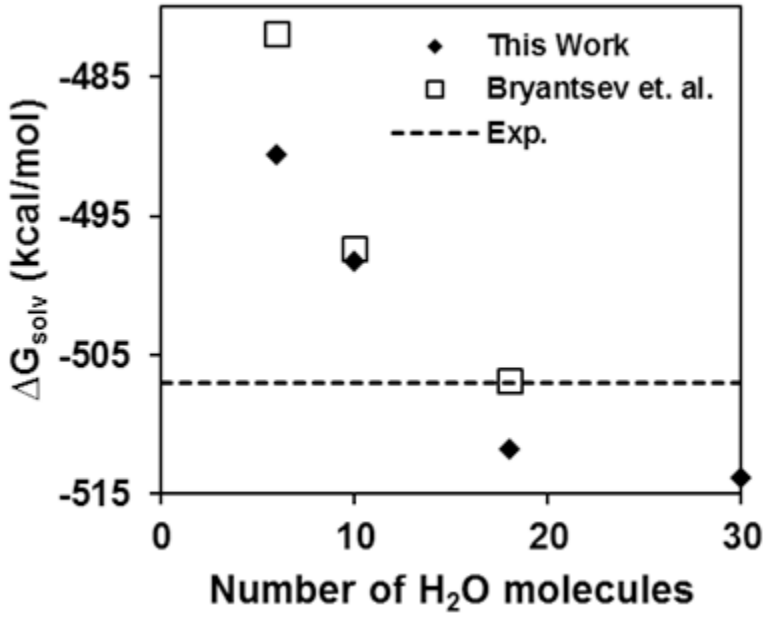

Figure 2. Solvation free energy of Cu^{2+} as a function of the number of water molecules.

The most stable structure of $[Cu(H_2O)_n]^{2+}$ after DFT optimization for n=6, 10, 18, and 30 are shown in Figure 3a-d, respectively. For n = 6, waters molecules form 5-coordinated complex around the Cu^{2+} ion in the elongated square pyramidal configuration. Meanwhile, larger size water clusters form 6-coordinated complexes. ABCluster did generate some six-coordinated complexes for n = 6, shown in Figure 3e. The absolute free energy difference between the most stable five-coordinated and six-coordinated complexes for n = 6 is 0.23 kcal/mol. These results are in agreement with the combined EXAFS and XANES studies of the hydration of Cu^{2+} by Chaboy and co-workers, which concluded five-coordinated and six-coordinated structures are indistinguishable and are likely to coexist in aqueous solution[29].

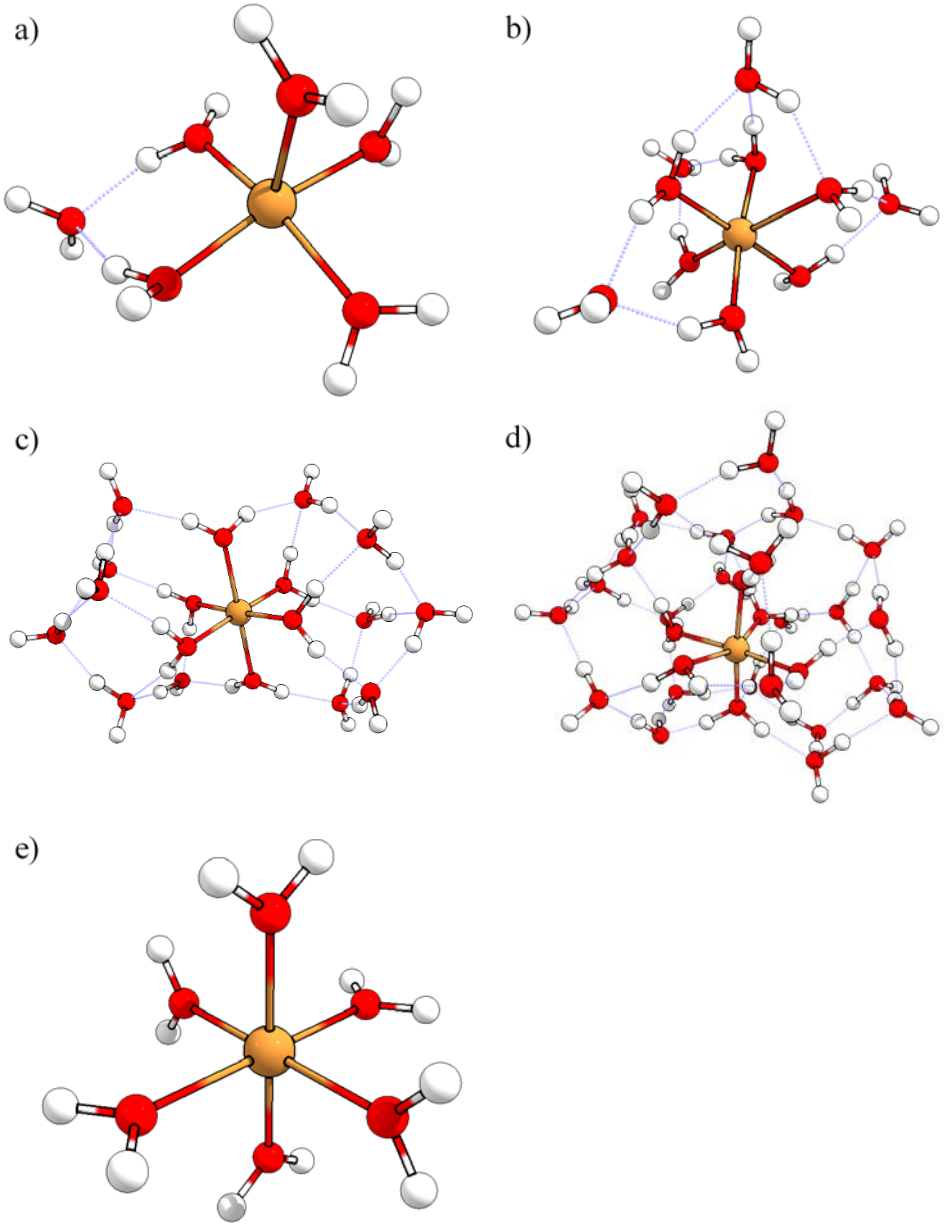

Figure 3. a-d) most stable structures of $[Cu(H_2O)_n]^{2+}$ after re-optimization at B3LYP/Def2-SVP level. e) six-coordinated structure of $[Cu(H_2O)_6]^{2+}$ complex.

2.3.2 Solvation free energies of other metal ions

This approach was also used to model absolute solvation energies for other metal cations. The general trends as seen for Cu^{2+} still hold for other metal cations (Figure 4). A benefit to this approach is the clusters are obtained automatically using ABCluster.

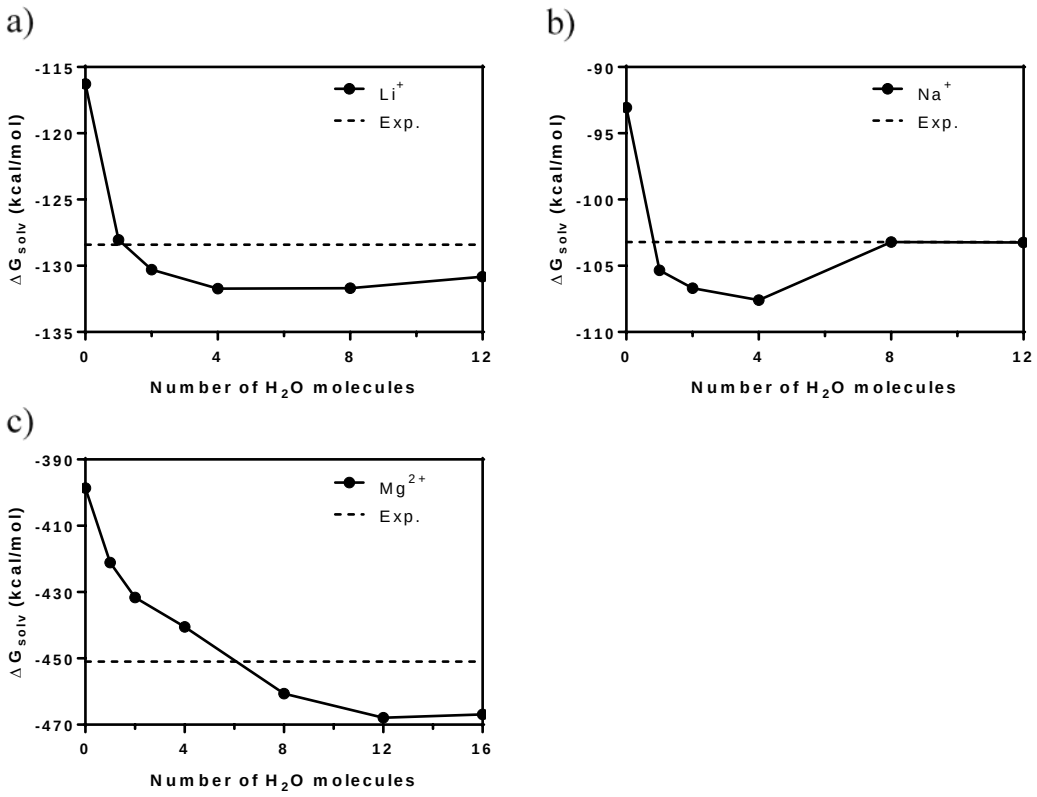

Figure 4. Solvation free energies of a) Li^+ b) Na^+ and c) Mg^{2+} as the function of the number of water molecules. Experimental data are taken from [28].

2.3.3 Coordination of chelating agents with metal ions

Our automated cluster-continuum modeling approach can also be used to determine realistic coordination environments of chelating agent binding to metal ions. Clioquinol (5-chloro-7-iodo-8-hydroxyquinoline) is a potential chelator for therapeutic treatment of Alzheimer's disease. In aqueous solution, the phenolic group of clioquinol is deprotonated and bind to Zn(II) to form a neutral binary metal-ligand complex ($ZnCQ_2$), and additional water molecules may coordinate to the complex. Rodriguez-Santiago's work[30] suggested that minimal cluster based DFT calculation with solvation correction yield incorrect tetrahedral coordination for complexation of Zn(II) with clioquinol, and that in ab initio molecular dynamics simulations, five-coordinated $Zn(CQ)_2(H_2O)$ and six-coordinated $Zn(CQ)_2(H_2O)_2$ coordinated complexes are quasi-degenerated structure and likely to exist in aqueous solution.

We generated clusters containing two clioquinol molecules, a Zn(II) atom, and either 2, 5, or 10 water molecules to investigate the coordination environment of Zn(II). For the coordination study, we used the lego module in the ABCluster code to generate the clustered complexes. This method allowed us to use an external quantum chemistry package to optimize and calculate the energy instead of relying on the CHARMM force field for ranking configurations. Structures generated with ABCluster code were relaxed using PM6 with Grimme's D3 dispersion as implemented in MOPAC[31,32]. The lowest 10 structures were re-optimized using the method described in the method section. Figure 5a shows the most stable five-coordinated $Zn(CQ)_2(H_2O)$ complex and Figure 5b shows the most six-coordinated $Zn(CQ)_2(H_2O)_2$ complex generated with our procedure. The $Zn(CQ)_2(H_2O)_2$ complex generated with our procedure is consistent with the $Zn(CQ)_2(H_2O)_2$ complex from the ab initio molecular dynamic simulation (AIMD) in Rodriguez-Santiago's work. This demonstrated that our method can capture similar micro solvation effect as

AIMD simulation. Given that AIMD simulation is computationally expensive, our method provides an alternative cost-effective and robust method to generate metal-ligand complexes.

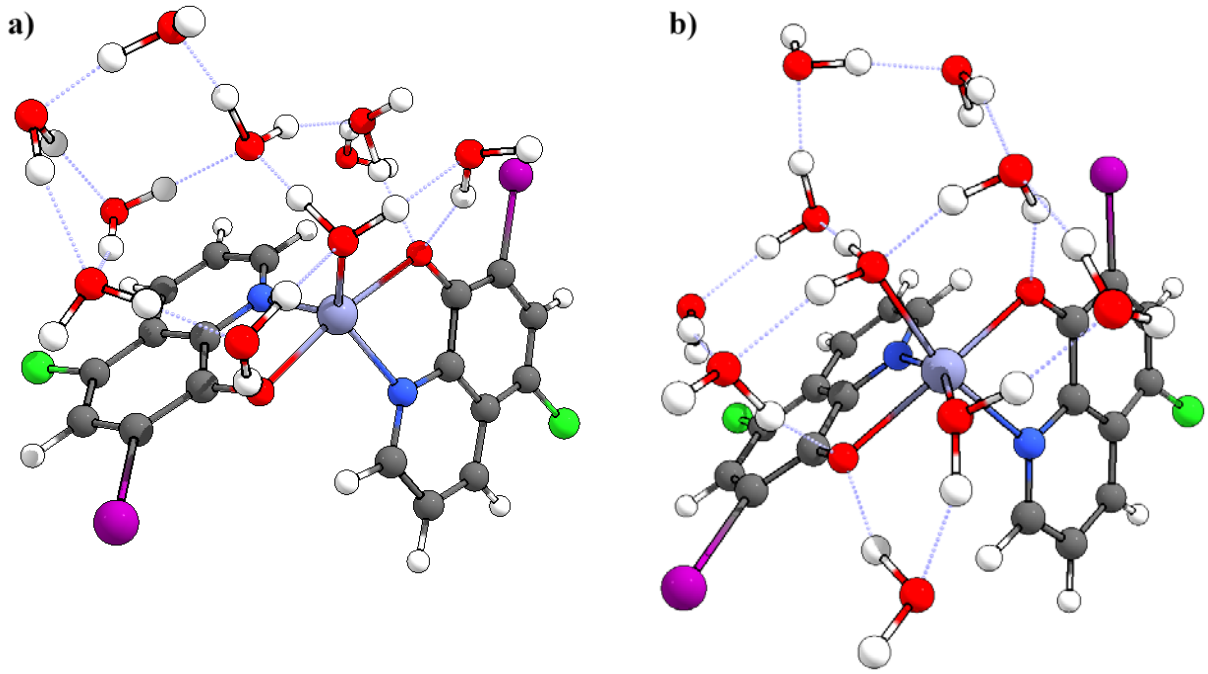

Figure 5. a) Five-coordinated and b) six-coordinated complexes of Zn^{2+} with 2 CQ ligands and water molecule generated with ABCluster.

2.4 CONCLUSION

In this chapter, we presented an automatable procedure to predict solvation free energies for ionic species. Our method used ABCluster code to generate hydrated cluster generation and mixed cluster continuum model to predict the solvation free energies. In addition, we also demonstrated that our method is capable of identifying stable metal-ligand complexes that are consistent with configurations generated with more computational expensive AIMD simulations.

3.0 ADJACENT LANTHANIDES SEPARATION

3.1 INTRODUCTION

Metals from the lanthanide series (La-Lu) are important ingredients in catalysts, hard magnets, phosphors, and lighting[33]. The separation of trivalent lanthanides ions (Ln^{3+}) is challenging because they possess similar ionic radii (the difference is only 16% across the series[34]). Current industrial processes use liquid-liquid extraction methods that rely on small differences in the ionic radii to separate adjacent lanthanides[35]. Lanthanides are then complexed with extractants (lipophilic ligands) and then separated based on their different propensities to partition between aqueous and organic phase[36]. The process requires multiple iteration steps to obtain satisfactory lanthanides purity, which consumes excessive amount of acids and bases and generates a vast quantity of secondary wastes. As the result, there is a need for new extractants that are effective and economical in separating adjacent lanthanides.

Computational-aid screening method can facilitate the discovery of new extractants. However, modeling complex systems that contain f-block electrons is particularly challenging[16,37]. Only a handful of studies in the literature was successful in predicting experimental binding energies and stability trend for lanthanide complexes[37,38]. In addition, most DFT studies focus on the separation of actinide-lanthanide and very few studies were conducted on adjacent lanthanide separation. Ivanov and Bryansev developed a computational approach that can accurately predict

the selectivity trend across the lanthanide series[39]. Their work uses 1:1 ligand/metal complex to predict the selectivity trends. In this work, we examine the effect of levels of theory and basis set sizes on the aqueous-phase binding energies and selectivity trends for 1:1 and 3:1 ligand/lanthanide complex systems. Extractants used in this study are shown in Figure 6.

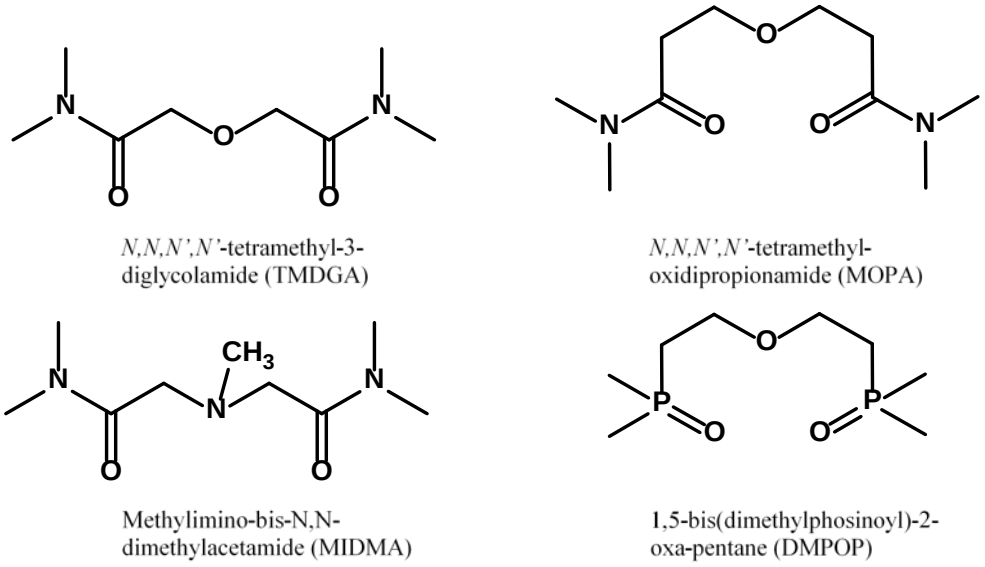

Figure 6. Ligands examined in this work.

3.2 COMPUTATIONAL DETAILS

Electronic structure calculations were performed with the Gaussian 09, revision D.01 program packages[40]. All DFT calculations were performed with B3LYP[23] functional. Trivalent lanthanides ions (La^{3+}, Gd^{3+}, and Lu^{3+}) were modeled using large-core (LC) relativistic effective core potential (RECP) and the related (7s6p5d)/[5s4p3d][41] basis sets. The standard 6-31+G* basis set was employed for light atoms and hydrogen. Frequency calculations were performed at the

B3LYP/LC/6-31+G* basis set to compute zero point energies and thermal correction using rigid rotor-harmonic oscillator approximation. Vibrational frequencies lower than 60cm^{-1} were raised to 60 cm^{-1}. This approximation was proposed by Truhlar[42] to correct the well-known breakdown of the harmonic oscillator model for the free energies of low-frequency vibration modes. Solvent effects beyond the first coordination shell were treated using IEF-PCM implicit solvation models[43]. Addition single-point energies were computed with the larger ma-def2-TZVP[24,44] basis set (diffuse basis sets were needed to accurately model the anion systems) and with M06L[45] and ωB97X-D3[46] functionals are calculated in ORCA[47]. The all-electron, zeroth-order regular approximation[48] (ZORA) (a scalar relativistic method) was also investigated.

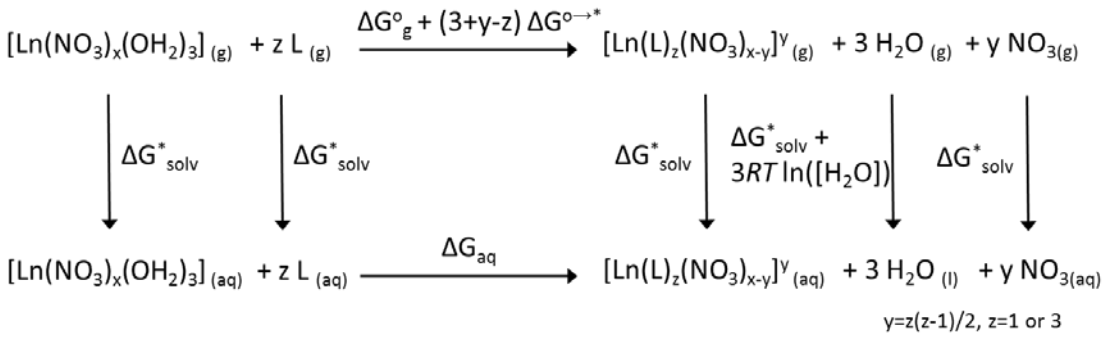

Figure 7. Thermodynamic cycle for calculating solvation free energies

Complexation free energies in aqueous solution, ΔG_{aq}, with ligands were calculated using the thermodynamic cycle shown in Figure 7. It was found that the computed hydration free energies of trivalent metal ions complexes with the total charge 3^+ are sensitive to small changes in the models and complex geometry, which could potentially introduce large uncertainties in the computed ΔG_{aq}. For single ligand complexes (ML), these issues can be greatly alleviated by introducing weakly coordinated nitrate anions. Nitrate was chosen as a counter ion in this study

because it is only weakly coordinated to Ln^{3+} ions (log K_1 = -0.1, 0.0, and 0.2 for La^{3+}, Gd^{3+}, and Lu^{3+}, respectively)[49]. Ln^{3+} ions in a tri-ligand complex (ML_3) are fully coordinated, and so no additional nitrate anions are necessary. From Figure 7, ΔG_{aq} is given by

$$\Delta G_{aq} = \Delta G_g^o + \Delta\Delta G_{solv}^* + (3 + y - z)\Delta G^{o\rightarrow *} + 3RT\ln([H_2O]) \quad (1)$$

Here, z = 1 for ML system and z = 3 for ML_3 system, and y = z(z – 1)/2. $\Delta G_g°$ is the free energy of complexation in the gas phase and $\Delta\Delta G^*_{solv}$ is the difference in the solvation free energies for a given reaction is

$$\Delta\Delta G_{solv}^* = \Delta G_{solv}^*([Ln(L)_3]^{3+}) + 3\Delta G_{solv}^*(H_2O) + y\Delta G_{solv}^*(NO_3) - z\Delta G_{solv}^*([Ln(L)_3]^{3+}) - \Delta G_{solv}^*(L_3) \quad (2)$$

The standard state correction, $\Delta G^{\circ\rightarrow *}$, represents the change in the free energy of transfer of 1 mol of solute from the gas phase at the standard state of 1 atm to the aqueous phase at a standard state of 1 M.

$$\Delta G^{o\rightarrow *} = -T\Delta S^{o\rightarrow *} = RT\ln(V°/V^*) = RT\ln(24.46) = 1.89\ \text{kcal/mol}\ (T = 298.15\ \text{K}) \quad (3)$$

Equation 3 is applied to each gas-phase reactant and product results in the correction given in the upper leg of the thermodynamic cycle shown in Figure 7. With water, an additional correction, RT ln([H_2O]) = 2.38 kcal/mol per molecule of water, is needed so that the pure solvent $H_2O_{(l)}$ is adopted as the reference state for the solvent in the lower leg of the thermodynamic cycle. This correction represents a free energy change associated with moving a solvent from a standard-state solution phase concentration of 1 M to standard state of the pure liquid, 55.34M.

Selectivity for two Ln^{3+} ions in aqueous solution is the difference between their complexation free energies. The thermodynamic cycle in Figure 8 was used to compute the selectivity trend across the lanthanide series. $\Delta\Delta G_{aq}(La^{3+}/Ln^{3+})$ corresponds to the selectivity for La^{3+} over Ln^{3+} for each ligand, L.

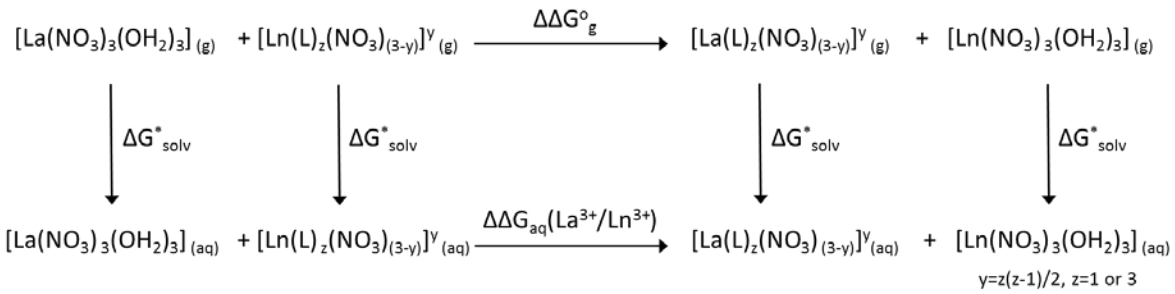

Figure 8. Thermodynamic cycle for calculating La^{3+}/Ln^{3+} Selectivity

3.3 RESULTS AND DISCUSSION

3.3.1 Aqueous binding energies and selectivity with 1:1 ligand/metal complex

Table 1 summarizes the binding energies in aqueous solution (ΔG_{aq}), calculated using the thermodynamic cycle in Figure 6, for 1:1 ligand/metal complexes of La^{3+}, Gd^{3+}, and Lu^{3+} with ligands in Figure 6. The ΔG_{aq} values of lanthanides bound to TMDGA, MIDMA, and DMPOP calculated at the B3LYP/6-31+G*/LC in ORCA are the same as those calculated in GAUSSIAN 09. The ΔG_{aq} values are about 3 kcal/mol more negative when using the larger ma-def2-TZVP basis set. The RI approximation improves the computation efficiency but only negligibly affects the calculated ΔG_{aq} (0.1 kcal/mol difference between B3LYP/ma-def2-TZVP and B3LYP/ma-def2-TZVP/RI). For example, ORCA took approximately 69 minutes to complete a single-point energy calculation with B3LYP/ma-def2TZVP/LC method on the TMDGA and Gd^{3+} complex, but the same calculation with RI approximation turned on completed in just 6 minutes. The ΔG_{aq} value calculated with ωB97x-d3 are more negative compared to values obtained using the B3LYP and M06-L functionals. The all-electron ZORA method yields similar ΔG_{aq} as using large-core

RECP. We conclude that different levels of theory and basis sets can affect relative binding energies for 1:1 complexes on the order of ~5 kcal/mol. Notably, there is almost no difference in binding energies using the RECP and the all electrons basis set.

Table 1. Summary of 1:1 ligand/metal complex with La^{3+}, Gd^{3+}, and Lu^{3+} at different levels of theory.

1:1 Complexes	Binding energies (ΔG_{aq})					
Ligands	TMDGA			MOPA		
Level of theory	La^{3+}	Gd^{3+}	Lu^{3+}	La^{3+}	Gd^{3+}	Lu^{3+}
B3LYP/6-31+G*/LC/G09	-9.1	-11.4	-12.8	-4.6	-5.3	-7.6
B3LYP/6-31+G*/LC	-9.1	-11.7	-13.0	-4.6	-5.5	-7.6
B3LYP/ma-def2-TZVP/LC	-13.2	-15.8	-17.7	-8.4	-9.2	-11.7
B3LYP/ma-def2-TZVP/LC/RI	-13.2	-15.7	-17.6	-8.3	-9.1	-11.7
M06L/ma-def2-TZVP/LC/RI	-13.7	-14.6	-15.8	-12.4	-12.0	-14.4
ωB97x-d3/ma-def2-TZVP/LC/RI	-14.3	-15.1	-17.5	-14.1	-14.1	-16.9
B3LYP/ma-zora-def2-TZVP/Z/RI	-13.0	-15.6	-17.4	-7.8	-8.6	-11.1
Ligands	MIDMA			DMPOP		
Level of theory	La^{3+}	Gd^{3+}	Lu^{3+}	La^{3+}	Gd^{3+}	Lu^{3+}
B3LYP/6-31+G*/LC/G09	-8.6	-10.7	-11.5	-9.0	-10.9	-11.6
B3LYP/6-31+G*/LC	-8.6	-10.9	-11.5	-9.0	-11.2	-11.6
B3LYP/ma-def2-TZVP/LC	-12.8	-15.1	-16.2	-12.0	-14.2	-15.3
B3LYP/ma-def2-TZVP/LC/RI	-12.8	-15.1	-16.2	-11.9	-14.1	-15.2
M06L/ma-def2-TZVP/LC/RI	-14.2	-15.1	-15.9	-12.8	-13.7	-12.2
ωB97x-d3/ma-def2-TZVP/LC/RI	-15.0	-16.2	-17.7	-16.9	-18.0	-18.6
B3LYP/ma-zora-def2-TZVP/Z/RI	-12.3	-14.7	-15.7	-11.6	-13.8	-15.2

G09 are energies calculated using Gaussian 09. Other energies are computed using ORCA. LC denotes the use of large core RECP for lanthanide ions, and Z denotes the use of all electron basis sets with ZORA.

A negative $\Delta\Delta G_{aq}(La^{3+}/Ln^{3+})$ indicates that the ligand binds more strongly to La^{3+} than its counterpart. A more negative $\Delta\Delta G_{aq}(La^{3+}/Lu^{3+})$ value compared to $\Delta\Delta G_{aq}(La^{3+}/Gd^{3+})$ value means that the ligand binds more strongly toward the lighter lanthanide. Despite differences in the binding energies, different basis sets with the B3LYP functional give similar magnitudes and selectivity trends. No experimental selectivity is available for MIDA, but the calculated selectivity trends for TMDGA and DMPOP are consistent with experimental trends, as shown in Table 2. Our

calculation shows that ligand MOPA is more selective for heavier lanthanide ions, but this trend is directly opposite to the experimental trend[50-54]. Since members of the TMDGA extractant families were reported to form a tris-complexes with lanthanides ions[51], we tentatively attribute the qualitative disagreement due to the 1:1 ligand/metal complex model as being inadequate for describing the selectivity trends. To better validate this hypothesis, we examined the binding energies for the full 3:1 ligand/metal complex.

Table 2. Summary of selectivity trends calculated with the 1:1 ligand/metal complex with different levels of theory. Negative selectivity, $\Delta\Delta G_{aq}(La^{3+}/Ln^{3+})$, indicates the ligand preference to bind with the lighter La^{3+} ion.

1:1 Complexes	Selectivity ($\Delta\Delta G_{aq}(La^{3+}/Ln^{3+})$)			
Ligands	TMDGA		MOPA	
Level of theory	La^{3+}/Gd^{3+}	La^{3+}/Lu^{3+}	La^{3+}/Gd^{3+}	La^{3+}/Lu^{3+}
B3LYP/6-31+G*/LC/G09	2.3	3.7	0.7	3.0
B3LYP/6-31+G*/LC	2.3	3.8	0.7	3.1
B3LYP/ma-def2-TZVP/LC	2.6	4.5	0.8	3.3
B3LYP/ma-def2-TZVP/LC/RI	2.6	4.5	0.8	3.3
M06L/ma-def2-TZVP/LC/RI	0.9	2.2	-0.4	2.0
ωb97x-d3/ma-def2-TZVP/LC/RI	0.8	3.2	-0.1	2.8
B3LYP/ma-zora-def2-TZVP/Z/RI	2.6	4.4	0.8	3.3
Experimental trend	$0 < La^{3+}/Gd^{3+} < La^{3+}/Lu^{3+}$		$La^{3+}/Lu^{3+} < La^{3+}/Gd^{3+} < 0$	
Ligands	MIDMA		DMPOP	
Level of theory	La^{3+}/Gd^{3+}	La^{3+}/Lu^{3+}	La^{3+}/Gd^{3+}	La^{3+}/Lu^{3+}
B3LYP/6-31+G*/LC/G09	2.1	2.9	1.9	2.6
B3LYP/6-31+G*/LC	2.1	2.9	2.0	2.6
B3LYP/ma-def2-TZVP/LC	2.3	3.4	2.2	3.3
B3LYP/ma-def2-TZVP/LC/RI	2.3	3.4	2.2	3.3
M06L/ma-def2-TZVP/LC/RI	0.9	1.7	0.9	-0.6
ωB97X-D3/ma-def2-TZVP/LC/RI	1.3	2.7	1.1	1.7
B3LYP/ma-zora-def2-TZVP/Z/RI	2.6	4.4	0.8	3.3
Experimental trend	---------		$0 < La^{3+}/Gd^{3+} < La^{3+}/Lu^{3+}$	

G09 are energies calculated using Gaussian 09. Other energies are computed using ORCA. LC denotes the use of large core RECP for lanthanide ions, and Z denotes the use of all electron basis sets with ZORA.

3.3.2 Aqueous binding energies and selectivity with 3:1 ligand/metal complex

From Table 3, similar to what was shown in Table 1, the ΔG_{aq} values calculated with ORCA are similar to the ΔG_{aq} value calculated with Gaussian 09. The ΔG_{aq} value computed with smaller 6-31+G* basis set are comparable to the ΔG_{aq} values calculated with the larger ma-def2-TZVP basis set at the B3LYP level of theory for TMDGA and MIDMA. Binding energies calculated with the M06-L functional are more positive by ~15 kcal/mol compared than the energies calculated with the B3LYP functional for TMDGA, MIDMA, and DMPOP. In contrast, ωB97X-D3 energies are more negative than the B3LYP energies by up to ~25 kcal/mol. For MOPA, M06-L functional gives slightly more negative binding energies than the B3LYP functional. The ZORA method binding energies are about 2-3 kcal/mol more positive than the calculations using a large-core RECP in most cases. This contrasts with the data reported in Table 1 where there was no notable difference between data from the RECP and all electron ZORA calculations.

Table 3. Summary of 3:1 ligand/metal complex with La^{3+}, Gd^{3+}, and Lu^{3+} at different levels of theory.

3:1 Complexes	Binding energies (ΔG_{aq})					
Ligands	TMDGA			MOPA		
Level of theory	La^{3+}	Gd^{3+}	Lu^{3+}	La^{3+}	Gd^{3+}	Lu^{3+}
B3LYP/6-31+G*/LC/G09	-27.9	-33.6	-35.8	-7.8	-5.8	-2.0
B3LYP/6-31+G*/LC	-28.0	-34.0	-35.9	-7.8	-6.1	-2.0
B3LYP/ma-def2-TZVP/LC	-28.5	-34.2	-36.4	-6.5	-4.6	-0.8
B3LYP/ma-def2-TZVP/LC/RI	-28.7	-34.3	-36.6	-6.6	-4.7	-0.5
M06L/ma-def2-TZVP/LC/RI	-8.3	-13.7	-16.6	-5.3	-6.3	-5.3
ωB97X-D3/ma-def2-TZVP/LC/RI	-28.9	-35.1	-38.6	-28.9	-30.6	-27.6
B3LYP/ma-zora-def2-TZVP/Z/RI	-26.2	-31.6	-34.0	-2.4	0.1	4.3
Ligands	MIDMA			DMPOP		
Level of theory	La^{3+}	Gd^{3+}	Lu^{3+}	La^{3+}	Gd^{3+}	Lu^{3+}
B3LYP/6-31+G*/LC/G09	-25.3	-28.2	-28.3	-26.7	-30.9	-33.9
B3LYP/6-31+G*/LC	-25.3	-28.4	-28.1	-26.9	-31.3	-34.0
B3LYP/ma-def2-TZVP/LC	-25.0	-27.8	-28.1	-22.2	-26.5	-29.9
B3LYP/ma-def2-TZVP/LC/RI	-25.1	-27.9	-28.0	-21.8	-26.0	-29.4
M06L/ma-def2-TZVP/LC/RI	-13.5	-16.7	-17.7	-6.2	-9.6	-14.1
ωB97X-D3/ma-def2-TZVP/LC/RI	-33.6	-38.8	-39.4	-37.9	-43.9	-48.8
B3LYP/ma-zora-def2-TZVP/Z/RI	-21.7	-24.6	-25.0	-20.6	-24.1	-27.9

G09 are energies calculated using Gaussian 09. Other energies are computed using ORCA. LC denotes the use of large core RECP for lanthanide ions, and Z denotes the use of all electron basis sets with ZORA.

The selectivity trends estimated with the 3:1 ligand/metal complex are summarized in Table 4. The selectivity trends predicted with the 3:1 ligand/metal complexes are now consistent with available experimental trends including for the MOPA ligand, which the 1:1 ligand/metal model failed to predict. Selectivity magnitudes and trends are also consistent with each other for different basis sets at the B3LYP functional. In addition, the all electron ZORA method produces similar selectivity magnitudes and trend as the large-core RECP. The M06-L and ωB97X-D3 functionals correctly predict the selectivity trends for TMDGA and DMPOP but failed to predict the trend for MOPA.

Table 4. Summary of 3:1 ligand/metal complex with La^{3+}, Gd^{3+}, and Lu^{3+} at different levels of theory. Negative selectivity, $\Delta\Delta G_{aq}(La^{3+}/Ln^{3+})$, indicates the ligand preference to bind with the lighter La^{3+} ion.

3:1 Ligand metal complexes	Selectivity ($\Delta\Delta G_{aq}(La^{3+}/Ln^{3+})$)			
Ligands	TMDGA		MOPA	
Level of theory	La^{3+}/Gd^{3+}	La^{3+}/Lu^{3+}	La^{3+}/Gd^{3+}	La^{3+}/Lu^{3+}
B3LYP/6-31+G*/LC/G09	5.7	7.9	-2.0	-5.8
B3LYP/6-31+G*/LC	6.0	7.9	-1.7	-5.8
B3LYP/ma-def2-TZVP/LC	5.6	7.9	-1.9	-5.7
B3LYP/ma-def2-TZVP/LC/RI	5.6	7.8	-1.9	-6.0
m06L/ma-def2-TZVP/LC/RI	5.3	8.3	0.9	-0.1
ωB97X-D3/ma-def2-TZVP/LC/RI	6.2	9.6	1.7	-1.3
B3LYP/ma-zora-def2-TZVP/Z/RI	5.4	7.8	-2.5	-6.7
Experimental trend	$0 < La^{3+}/Gd^{3+} < La^{3+}/Lu^{3+}$		$La^{3+}/Lu^{3+} < La^{3+}/Gd^{3+} < 0$	
Ligands	MIDMA		DMPOP	
Level of theory	La^{3+}/Gd^{3+}	La^{3+}/Lu^{3+}	La^{3+}/Gd^{3+}	La^{3+}/Lu^{3+}
B3LYP/6-31+G*/LC/G09	2.9	2.9	4.1	7.1
B3LYP/6-31+G*/LC	3.1	2.7	4.4	7.2
B3LYP/ma-def2-TZVP/LC	2.8	3.1	4.3	7.6
B3LYP/ma-def2-TZVP/LC/RI	2.8	2.8	4.2	7.7
m06L/ma-def2-TZVP/LC/RI	3.3	4.2	3.4	7.9
ωB97X-D3/ma-def2-TZVP/LC/RI	5.2	5.8	6.0	10.9
B3LYP/ma-zora-def2-TZVP/Z/RI	2.9	3.3	3.5	7.3
Experimental trend	---		$0 < La^{3+}/Gd^{3+} < La^{3+}/Lu^{3+}$	

G09 are energies calculated using Gaussian 09. Other energies are computed using ORCA. LC denotes the use of large core RECP for lanthanide ions, and Z denotes the use of all electron basis sets with ZORA.

3.4 CONCLUSION

In summary, our data indicates that the 3:1 ligand/metal model is better suited to predict the selectivity trends across the lanthanide series than the 1:1 ligand/metal model. Based on the extractants examined, the B3LYP functional appears to better predict the selectivity trends than M06-L and ωB97X-D3 functionals. We conclude that for a fast and efficient screening of lanthanide extractant selectivities, the B3LYP/6-31+G*/LC level of theory is adequate. For more

reliable binding energies, ZORA method should be used since these values are about 3 kcal/mol different than values obtained using the large-core RECP.

4.0 POLYMERIZATION MECHANISM OF ISOBUTYLENE

4.1 INTRODUCTION

Polyisobutylenes (PIBs) are essential for a vast range of applications due to their desired properties at different ranges of molecular weight (M_n). High Low molecular weight PIBs ($M_n > 10^5$ g mol^{-1}) have a high viscosity, and they are commonly used for the synthesis of rubber products such as chewing gum and car tires[55,56]. Medium molecular weight PIBs ($5 \times 10^3 < M_n < 3 \times 10^4$ g mol^{-1}) vary from viscous liquid to tacky semisolids and can be found in sealant and caulking products. Low molecular weight PIBs ($M_n < 5 \times 10^3$ g mol^{-1}) are used as precursors for making adhesives and lubricants, and as additives for motor oils and fuels. Industrially, molecular weights of PIBs are temperature controlled. PIBs are produced through cationic polymerization, and the process is exothermic in nature. Thus, low molecular weight PIBs are polymerized between -40 to 10°C, and high molecular weight PIBS are synthesized at even lower temperatures, -100 to -90°C[57].

Cationic polymerization involves the use of a Lewis acid as the catalyst (e.g $AlCl_3$, BF_3, $TiCl_4$)[55] and a proton donor, such as water, hydrogen halide, and alcohol. A proton donor is crucial for the polymerization of isobutylene. In fact, no reaction is observed when BF_3 is added directly to dry isobutylene (IB), but polymerization occurs almost instantaneously when trace quantities of water are added to the mixture[58]. The choice of catalysts also greatly affect the terminal groups on

PIBs. The $AlCl_3$-catalyzed process produces conventional PIBs, which contains up to 90% of internal double bond end groups(trisubstituted, tetrasubstituted), shown in Figure 1a. Meanwhile, BF_3-catalyzed PIBs have a high content of terminal vinylidene (exo) groups, shown in Figure 1b, which are also known as highly reactive (HR) PIBs.

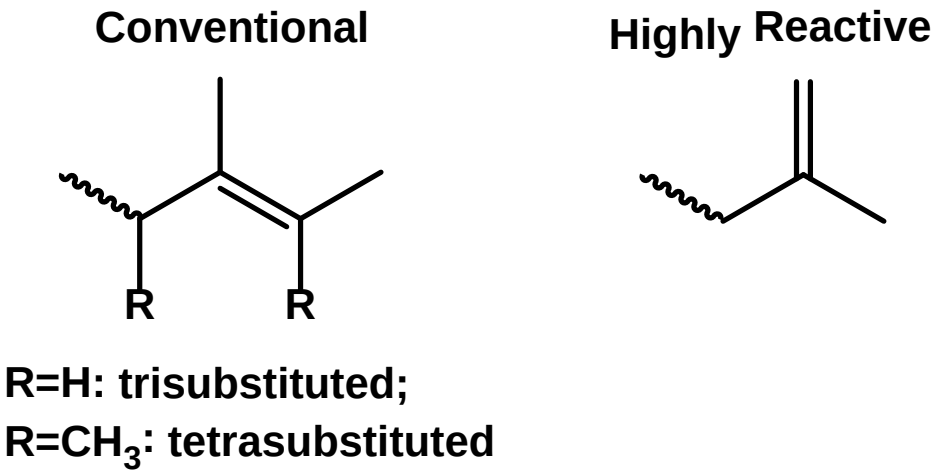

Figure 9. Terminal group of a) conventional and b) highly reactive PIBs

The processes of making PIBs have been around for over 50 years, but the knowledge on polyisobutylene reaction mechanism is limited because the reaction is experimentally difficult to study. Some experimental studies on the reaction mechanism for PIB with different catalysts are available in the literature[56,57,59,60], but there is no direct molecular-level information on the reaction mechanisms producing conventional and HR PIBs. In this study, quantum mechanical density functional theory is used to study the thermodynamics and reaction energetics of elementary reaction steps of PIB polymerization. This study focused on the reaction mechanism with $AlCl_3/H_2O$ co-initiator.

4.2 COMPUTATIONAL DETAILS

Electronic structure calculations were performed with the ORCA program packages[47]. Optimizations were performed at BP86[61]/def2-SVP level of theory with the RI-J approximation[25] and Grimme's D3 dispersion. Frequency calculations were performed at the same level of theory and basis set to verify that geometries were at the minima and to compute zero point energies and thermal corrections. Vibrational frequencies lower than 60 cm^{-1} were raised to 60 cm^{-1}. This approximation was proposed by Truhlar[42] to correct the well-known breakdown of the harmonic oscillator model for free energies of low-frequency vibration modes. Single-point energy calculations were performed at B3LYP[23]/def2-TZVP[24] basis set.

The single-ended growing string method (GSM), a transition state locating technique, written by Zimmerman, was used to generate reaction coordinates along reaction pathways. A detailed discussion of the growing string method can be found in [62,63]. The GSM invokes ORCA and utilizes the BP86 functional with the polarized 6-31G** basis set to provide the quantum mechanical gradients.

The gas phase Gibbs free energy (G_g) for each species at T = 298 K is computed from

$$G_g = E_{SCF} + ZPE + H - TS$$

where E_{SCF} is the single-point electronic energy calculated from DFT, ZPE is the zero-point energy, H is the change in enthalpy from 0 to 298 K, and S is the entropy at 298 K. The polymerization reaction takes place in pure IBs or with the presence of other C4 olefins, which are non-polar organic solvents. The dielectric constants (ε = 1 for vacuum) for these solvents are very

small (butane ε = 1.4, vs water ε = 80.4 at room temperature). As a result, gas phase reaction free energies were used to approximate the thermodynamics inside the actual process.

4.3 RESULTS AND DISCUSSION

4.3.1 Reaction Thermodynamics

A proposed mechanism for cationic polymerization of PIBs, involves the formation of co-initiator complex, as shown in Figure 10a[57,64]. The initiation step occurs when an IB approaches the $AlCl_3/H_2O$ complex and extract a proton from the water molecule. This results in $[AlCl_3OH]^-$ and IBH^+ complexes. The reaction is propagated by successive insertions of the IB monomer between the carbocation and $[AlCl_3OH]^-$ complex.

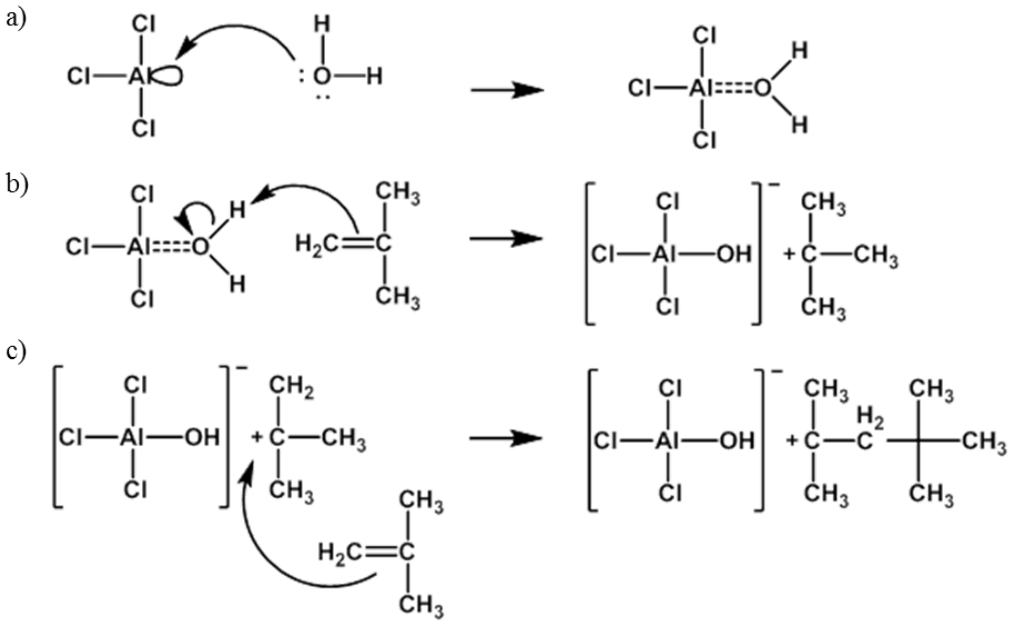

Figure 10. a) Proposed formation of co-initiator complex b) initiation step and c) propagation step for cationic polymerization of isobutylene

We examined each reaction step with $(AlCl_3)_n$ cluster sizes, n = 1, 2, 3 and 4. Most stable structures of $AlCl_3$ dimer, trimer, and tetramer were taken from Varga work and re-optimized with the levels of theory described in Section 4.2. Structures of these $AlCl_3$ clusters are shown in Figure 11. Figure 12 shows the reaction pathway investigated in this work with the $AlCl_3$ dimer. In Figure 10, the gas phase Gibbs free energy of formation (ΔG_g) of the $AlCl_3/H_2O$ co-initiator complex, I → II, at room temperature is -17.4 kcal/mol. This suggests that the formation of co-initiator complex is thermodynamically favorable. $AlCl_3$ dimer forms chlorine bridges to increase its structure stability. One of the chlorine bridge is broken off for the insertion of a water molecule on the aluminum to form the co-initiator complex, shown in Figure 12 (II). Although HCl can be used as a proton donor for PIB polymerization, the formation of HCl from the $AlCl_3/H_2O$ complex, II → III, is thermodynamically unfavorable (ΔG_g = 5.1 kcal/mol). Given that the polymerization process occurs below room temperature, we believe that HCl is unlikely to form in the reactor, which primarily contains pure IBs.

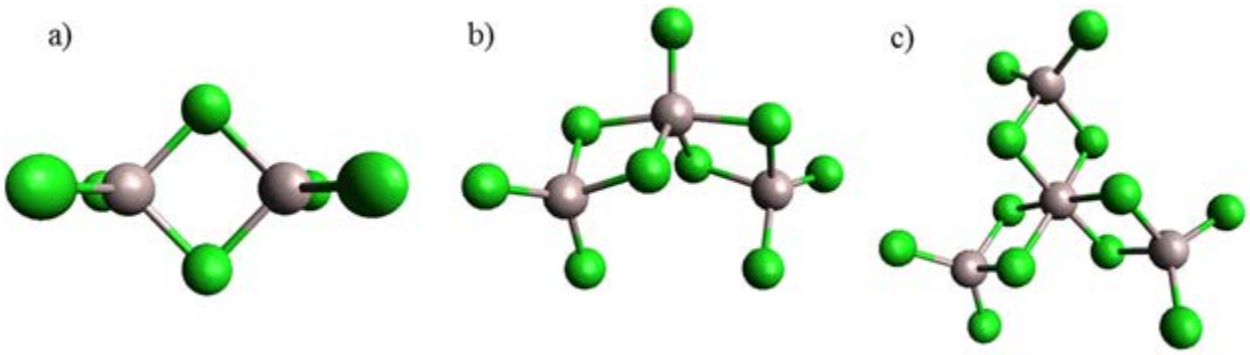

Figure 11. Most stable structure of $(AlCl3)_n$ cluster a) dimer b) trimer and c) tetramer

The addition of an IB monomer to the $AlCl_3/H_2O$ complex, Figure 12 II→ III, to form two infinitely separated charged species $AlCl_2OH^-$ and IBH^+ is extremely unfavorable, (ΔG_g = 88.0

kcal/mol). This is reasonable as charged species are unstable in non-polar solvents. In contrast, the addition of IB monomer to form $[AlCl_3OH]^-IBH^+$, II→ III, with the carbocation bound to the OH group is thermodynamically favorable (ΔG_g = -20.4 kcal/mol). Furthermore, the addition of the second IB monomer to the complex, V→ VI, is also favorable (ΔG_g = -20.4 kcal/mol). Reactions II→ III and V→ VI are the potential initiation and propagation steps, respectively. Table 5 summarizes the gas phase reaction energies for different $AlCl_3$ cluster sizes.

From Table 5, ΔG_g for the formation of $AlCl_3/H_2O$ complex, II → III, are all negatives indicating that the reaction is favorable at all $AlCl_3$ cluster sizes examined. The ΔG_g is most negative for the monomer of $AlCl_3$. In contrast, the ΔG_g value for forming HCl, II → III, is significantly more positive for the $AlCl_3$ monomer case and decreases with the increase in $AlCl_3$ cluster size. ΔG_g values for II → III reaction are very large for all $AlCl_3$ cluster sizes suggesting this reaction is unlikely to occur at room temperature. The first addition of IB to the $AlCl_3/H_2O$ complex is more favorable for the $AlCl_3$ dimer, but the ΔG_g values increase with the increase in $AlCl_3$ cluster size, which might be attributed to the steric effect. The addition of the second IB to the complex is favorable for all cases.

We have determined that the reactions I → II → V → VI are the most thermodynamically favorable steps to form IB-IBH^+. Next, we examine the reaction barriers for these reactions using the single-ended GSM.

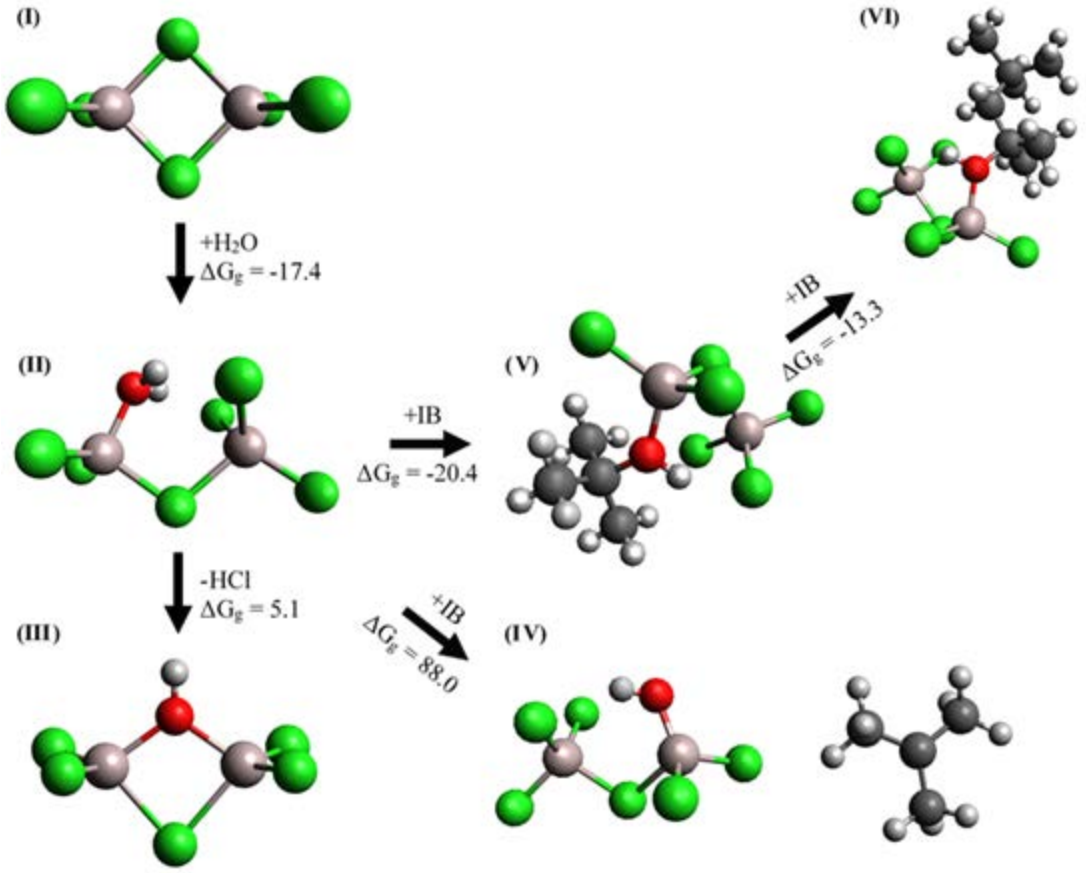

Figure 12. Gas phase Gibb free energies for various reactions. Energies are reported in kcal/mol

Table 5. Summary of gas phase reaction free energies, ΔGg, for reactions in Figure 12 with different $AlCl_3$ cluster size

Reactions	ΔG_g (kcal/mol)
(I) → (II)	
$A+H_2O \rightarrow AOH_2$	-23.3
$AA+H_2O \rightarrow AAOH_2$	-17.4
$AAA+H_2O \rightarrow AAAOH_2$	-16.8
$AAAA+H_2O \rightarrow AAAAOH_2$	-16.9
(II) → (III)	
$AOH_2 \rightarrow BOH + HCl$	26.2
$AAOH_2 \rightarrow ABOH + HCl$	5.1
$AAAOH_2 \rightarrow AABOH + HCl$	2.5
$AAAAOH_2 \rightarrow AAABOH + HCl$	-1.2
(II) → (IV)	
$AOH_2 + IB \rightarrow AOH^- + IBH^+$	102.3
$AAOH_2 + IB \rightarrow AAOH^- + IBH^+$	88.0
$AAAOH_2 + IB \rightarrow AAAOH^- + IBH^+$	89.4
$AAAAOH_2 + IB \rightarrow AAAAOH^- + IBH^+$	82.3
(II) → (V)	
$AOH_2 \rightarrow [AOH]^-IBH^+$	-19.0
$AAOH_2 \rightarrow [AAOH]^-IBH^+$	-20.4
$AAAOH_2 \rightarrow [AAAOH]^-IBH^+$	-18.8
$AAAAOH_2 \rightarrow [AAAAOH]^-IBH^+$	-16.4
(V) → (VI)	
$[AOH]^-IBH^+ + IB \rightarrow [AOH]^-IB\text{-}IBH^+$	-11.7
$[AAOH]^-IBH^+ + IB \rightarrow [AAOH]^-IB\text{-}IBH^+$	-13.3
$[AAAOH]^-IBH^+ + IB \rightarrow [AAAOH]^-IB\text{-}IBH^+$	-12.5
$[AAAAOH]^-IBH^+ + IB \rightarrow [AAAAOH]^-IB\text{-}IBH^+$	-14.2

A represents an $AlCl_3$, and B represents an $AlCl_2$

4.3.2 Predicting reaction pathway with GSM

Two simple reactions were first examined, the formation of $AlCl_3/H_2O$ complex and IB-IBH^+. Figure 13a) and 13c) are the input configurations we used and Figure 13b) and 13d) are the final configurations generated with the single-ended growing string method. The potential energy surfaces, shown in Figure 14, indicates no reactions barriers for both reactions. This is plausible

as $AlCl_3$ is extremely hydrophilic and carbocation on the IBH^+ is very reactive. In addition, no transition state was found for either reactions, which corroborates the barrierless reaction pathways. The ΔE_{rel} value for the formation of $AlCl_3/H_2O$ is -26 kcal/mol, and this consistent with the ΔG_g value of -23.3 kcal/mol calculated in the previous section.

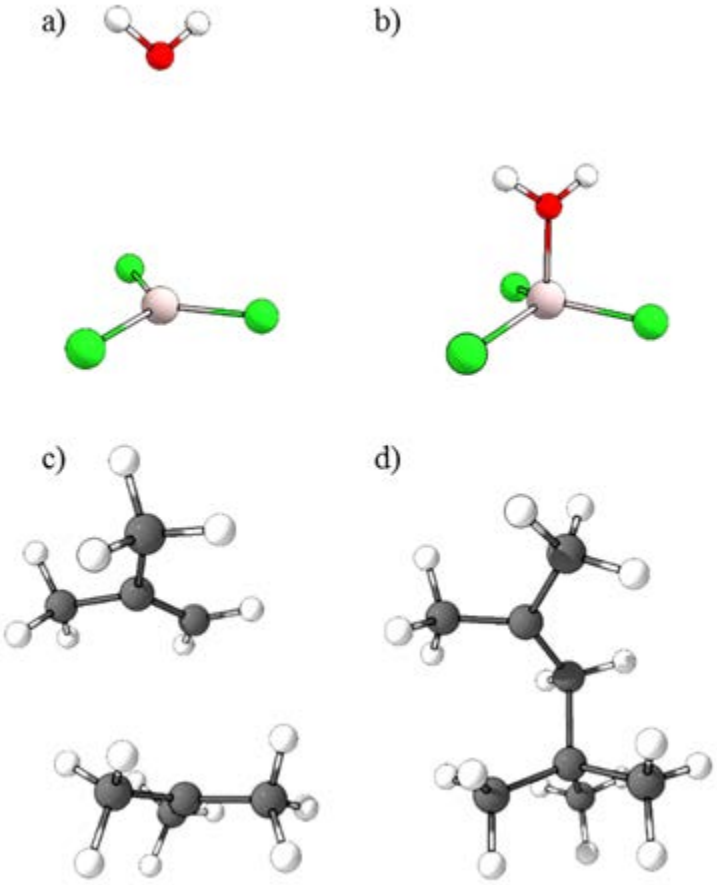

Figure 13. a) Initial configuration and b) final configuration for the formation of $AlCl_3OH_2$ complex generated with single-ended GSM at BP86/6-31G level. c) Initial starting configuration and d) final configuration for the reaction of IB+IBH^+.**

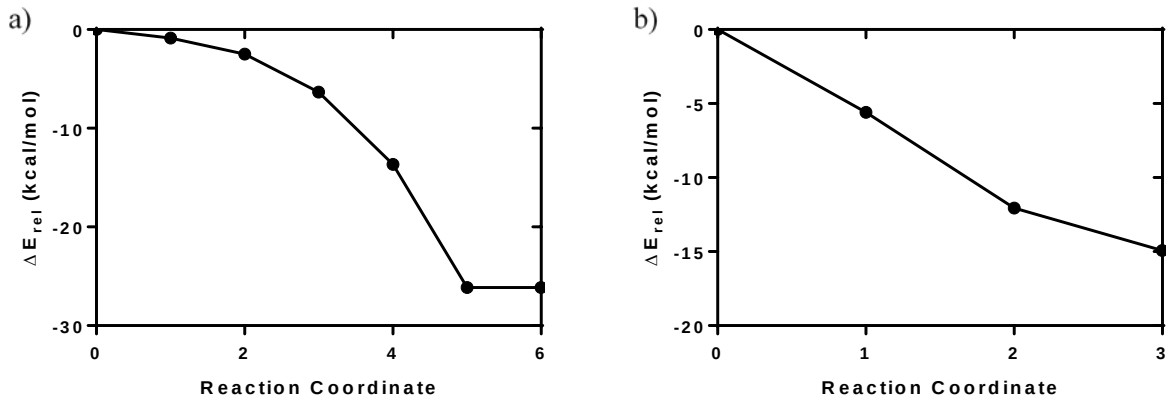

Figure 14. a) Potential energy surfaces for the formation of $AlCl_3OH_2$ complex and b) for the reaction of IB+IBH^+ calculated at B3LYP/def2-TZVP level

4.3.2.1 Initiation reaction pathway

Key configurations for the initiation step, addition of IB to the $(AlCl_3)_2/H_2O$ complex, are shown in Figure 15. At the initial configuration, shown in Figure 15a, hydrogen atoms on the water molecules are directed toward chlorine atoms. A local minimum intermediate, identified by GSM, shows a hydrogen atom rotated towards the alkene carbon on the approaching IB molecule. Figure 15c) shows a late transition state, where a proton has already transferred to the IB but is still in a close proximity with the oxygen atom. The IB maintains planar structures after the proton but then collapses as the carbocation binds to the oxygen, Figure 15d).

Potential energy surfaces for the initiation steps with different $AlCl_3$ cluster sizes are shown in Figure 16. In each reaction pathway, GSM located a local minimum configuration just before the high-energy transition state. The activation energies, E_a, are approximated as the difference between the transition state and the local minimum state. The relative reaction energies, ΔE_{rxn}, are computed as the difference between the product state and the local minimum state. These energies are summarized in Table 6.

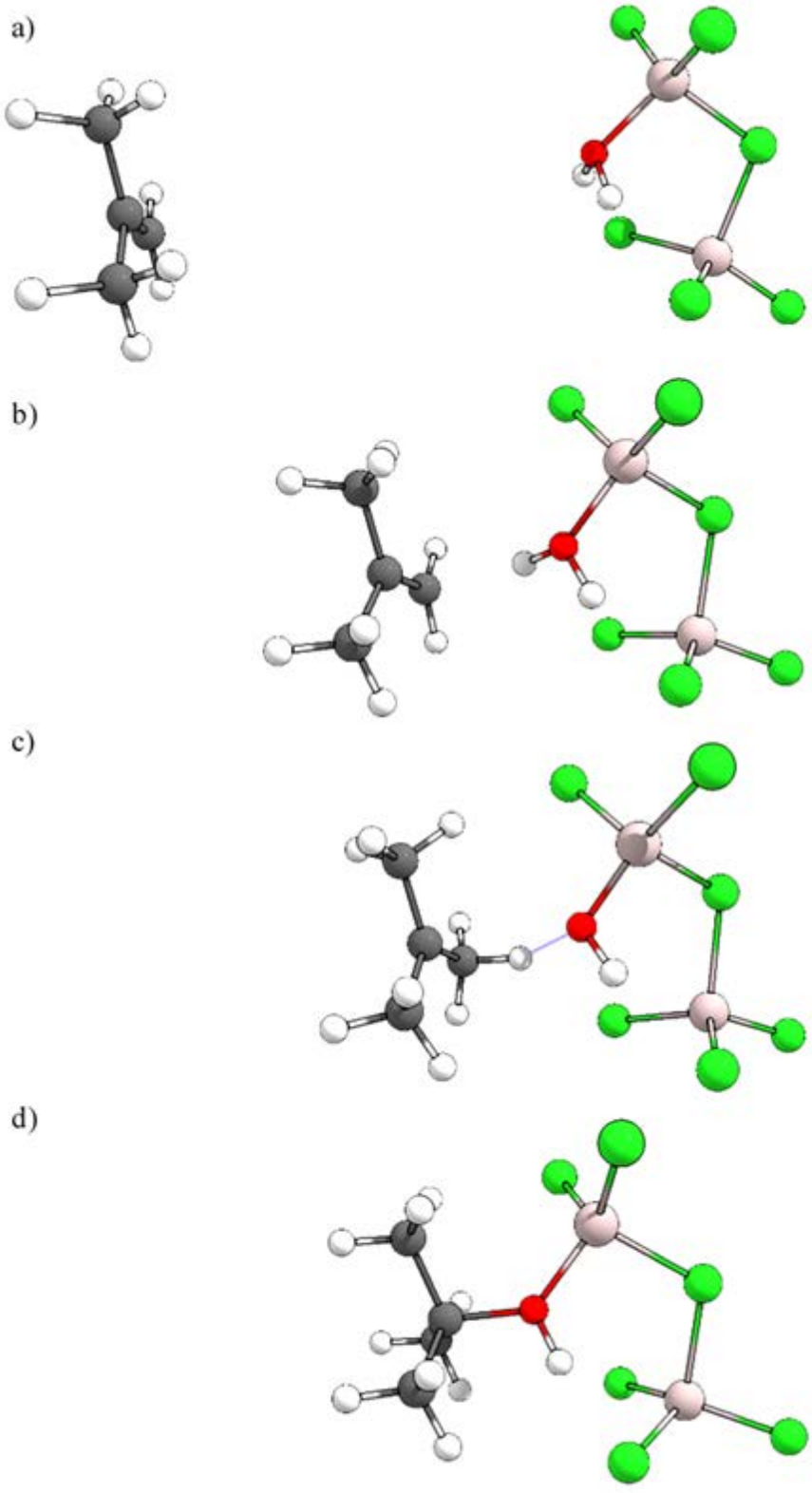

Figure 15. a) Initial configuration, b) transition state, c) local minimum configuration and d) final configuration for the initiation step

As seen from Figure 16 and Table 6, the $AlCl_3$ trimer system has the highest reaction barrier of 19.5 kcal/mol and $AlCl_3$ dimer system has the lowest reaction barrier of 14.8 kcal/mol. The proton transfer is responsible for these high reaction barriers. The overall reaction, however, is exothermic as all ΔE_{rxn} are negative, and the reaction with $AlCl_3$ dimer is the most exothermic with ΔE_{rxn} = -13.1 kcal/mol. The ΔE_{rxn} values are less negative for $AlCl_3$ trimer (-6.2 kcal/mol) and $AlCl_3$ tetramer (-1.4 kcal/mol). With very large E_a and relatively small ΔE_{rxn} values, the reaction pathways generated for $AlCl_3$ trimer and tetramer are unlikely to happen. Even for our lowest reaction barrier pathway, the $AlCl_3$ dimer reaction, the reaction barrier of 14.8 kcal/mol is relatively high for a reaction that occurs rapidly below room temperature. Nevertheless, we proceed with examining the propagation step.

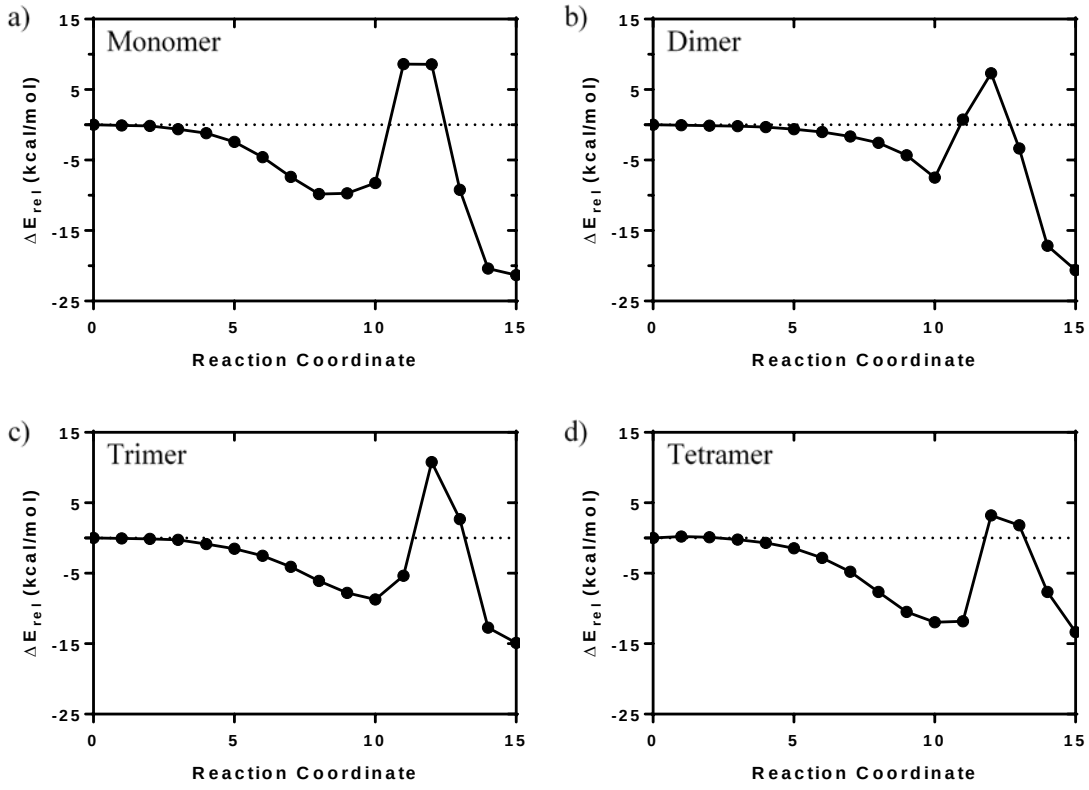

Figure 16. Potential energy surface for initiation step $(AlCl_3)_nOH_2$+IB→$[(AlCl_3)_nOH]^-IBH^+$ calculated at B3LYP/def2-TZVP level. a) monomer (n=1) b) dimer (n=2) c) trimer (n=3) d) tetramer (n=4).

Table 6. Activation energies (E_a) and relative reaction energies (ΔE_{rxn}) for the formation of $[A_nOH]^-IBH^+$ complex

Reactions	E_a	ΔE_{rxn}
$AOH_2 + IB \rightarrow [AOH]^-IBH^+$	18.5	-11.5
$AAOH_2 + IB \rightarrow [AAOH]^-IBH^+$	14.8	-13.1
$AAAOH_2 + IB \rightarrow [AAAOH]^-IBH^+$	19.5	-6.2
$AAAAOH_2 + IB \rightarrow [AAAAOH]^-IBH^+$	15.1	-1.4

4.3.2.2 Propagation reaction pathway

The propagation step involves the breaking of the C-O bond and the formation of the C^+-C bond and the new C-O bond, Figure 17. As the second IB approaches the complex, the IBH^+ is separated from the $(AlCl_3)_2OH^-$ complex. Carbocation forms a new bond with the alkene group on the second IB almost simultaneously as the OH^- forms a bond with the tertiary carbon on the second IB. The potential surface for the propagation step is shown in Figure 18.

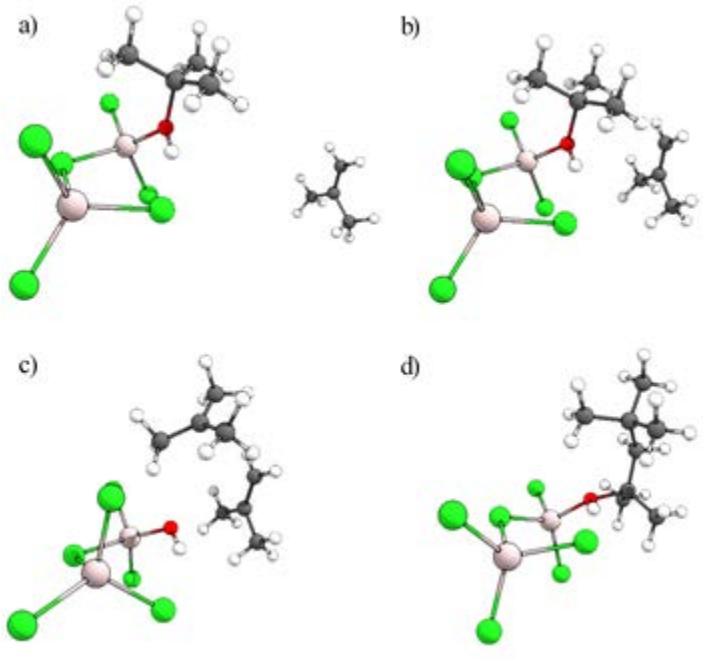

Figure 17. a) Initial configuration, b) transition state, c) local minimum configuration and d) final configuration for the propagation step

Again, the reaction barrier is relatively high (E_a = 34.1 kcal/mol). In this case, the high energy barrier is attributed to the breaking of the C-O bond. The overall reaction, however, is downhill in energy, ΔE_{rxn} = -9.3 kcal/mol. The propagation step is expected to have a low reaction barrier because polymerization reaction occurs very rapidly at low to moderate temperatures. Consequently, the high reaction barriers for the initiation and propagation steps lead us to believe that the pathway, II → V → VI, may not be consistent with experimental reaction conditions, indicating the existence of a more favorable pathway. Next, we examine the initiation step using intermediate III.

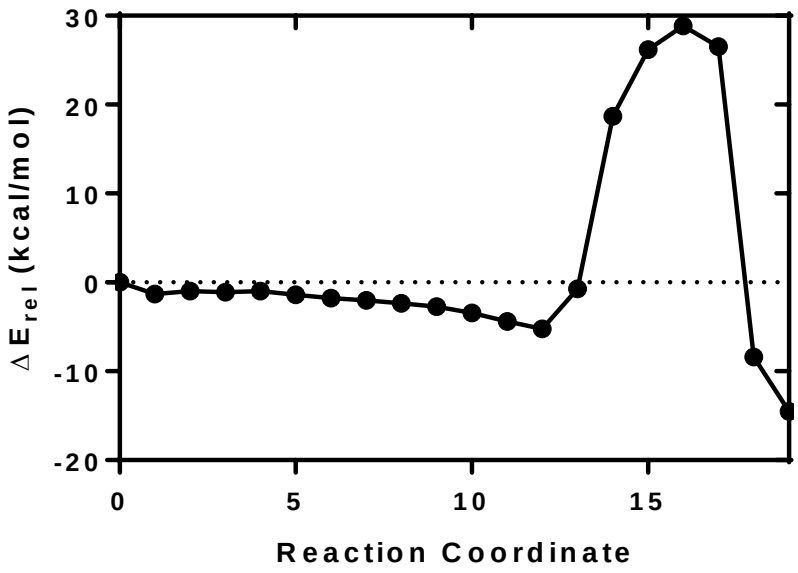

Figure 18. Potential energy surface for the propagation step, $[(AlCl_3)_2OH]^-$IBH+IB→$[(AlCl_3)_2OH]^-$IBIBH$^+$, calculated at B3LYP/def2-TZVP

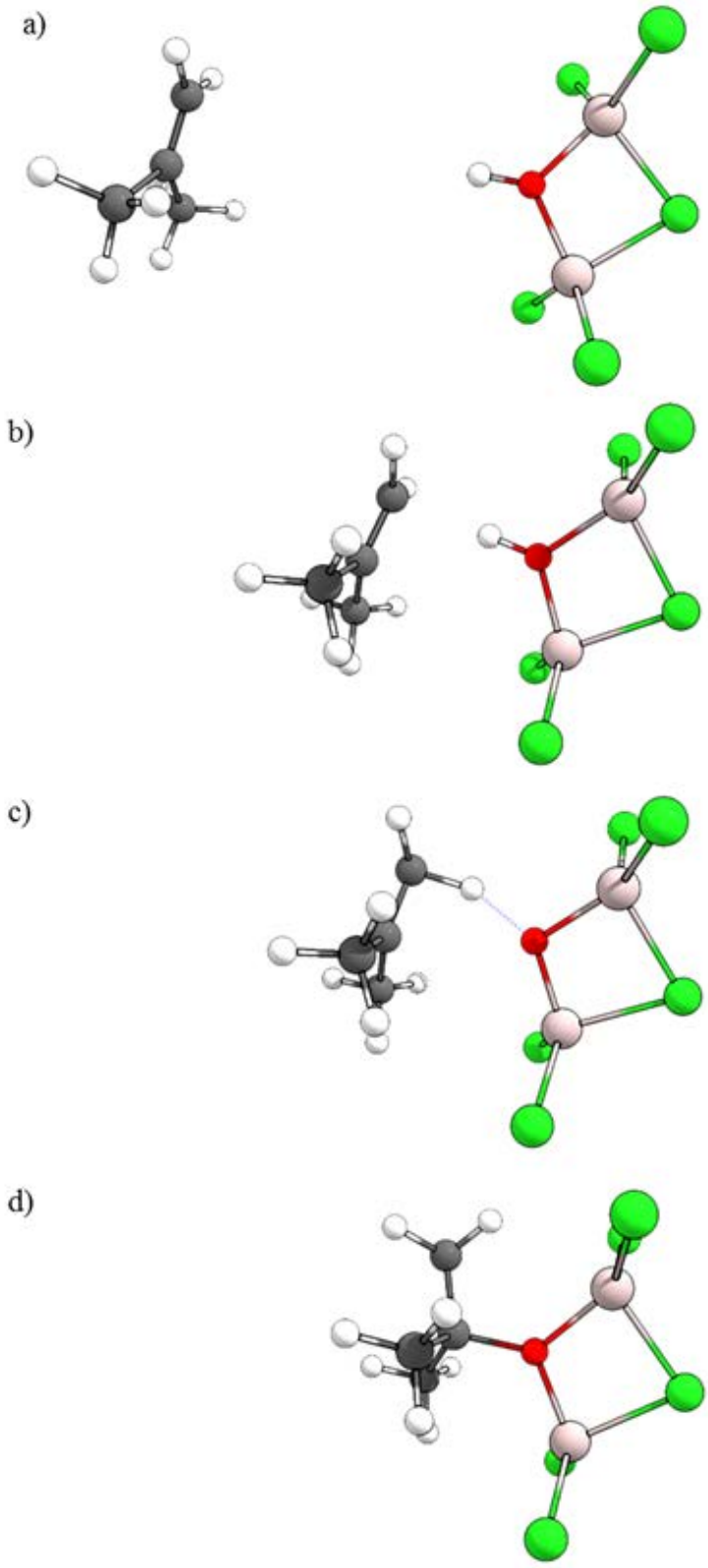

Figure 19. Initiation reaction intermediates with complex III in Figure 12. a) Initial state b) local minimum state c) transition state and d) product state.

4.3.2.3 Alternative reaction pathways

Key configurations for the initiation reaction with the complex III are shown in Figure 19. Similarly, this pathway proceeds with the transfer of the proton to the IB and then the formation of the C-O bond. As seen in Figure 20, the E_a for this reaction is 24.0 kcal/mol and the ΔE_{rxn} is -8.8 kcal/mol. The E_a value for the initiation reaction with complex III is almost 10 kcal/mol more positive than the E_a value with complex II. As the result, we believe this reaction pathway is unlikely for the given the experimental reaction conditions.

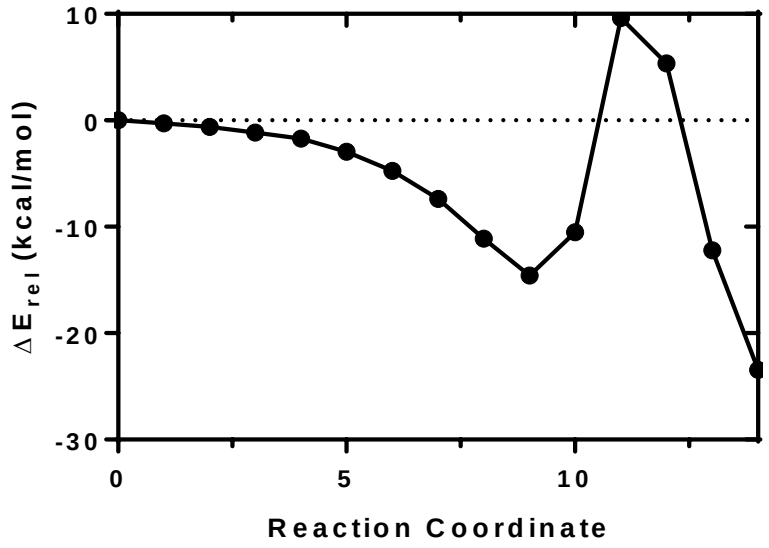

Figure 20. Potential energy surface for the initiation step with complex III, $AlCl_3AlCl_2OH+IB \rightarrow [AlCl_3AlCl_2OH]^-IBH^+$, calculated at B3LYP/def2-TZVP

Looking at the alternative $AlCl_3H_2O$ complexes, we found a potential co-initiator complex for IB polymerization. The complex is formed by adding an $AlCl_3$ to a complex of $AlCl_3H_2O$ monomer, as shown in Figure 21a. The oxygen atom in a water molecule has two lone pairs. Even after forming a complex with an $AlCl_3$ monomer, oxygen still has an extra lone pair, which is capable of forming a dative bond with another $AlCl_3$. Figure 21b shows the local minimum state just before the formation of the Al-O bond.

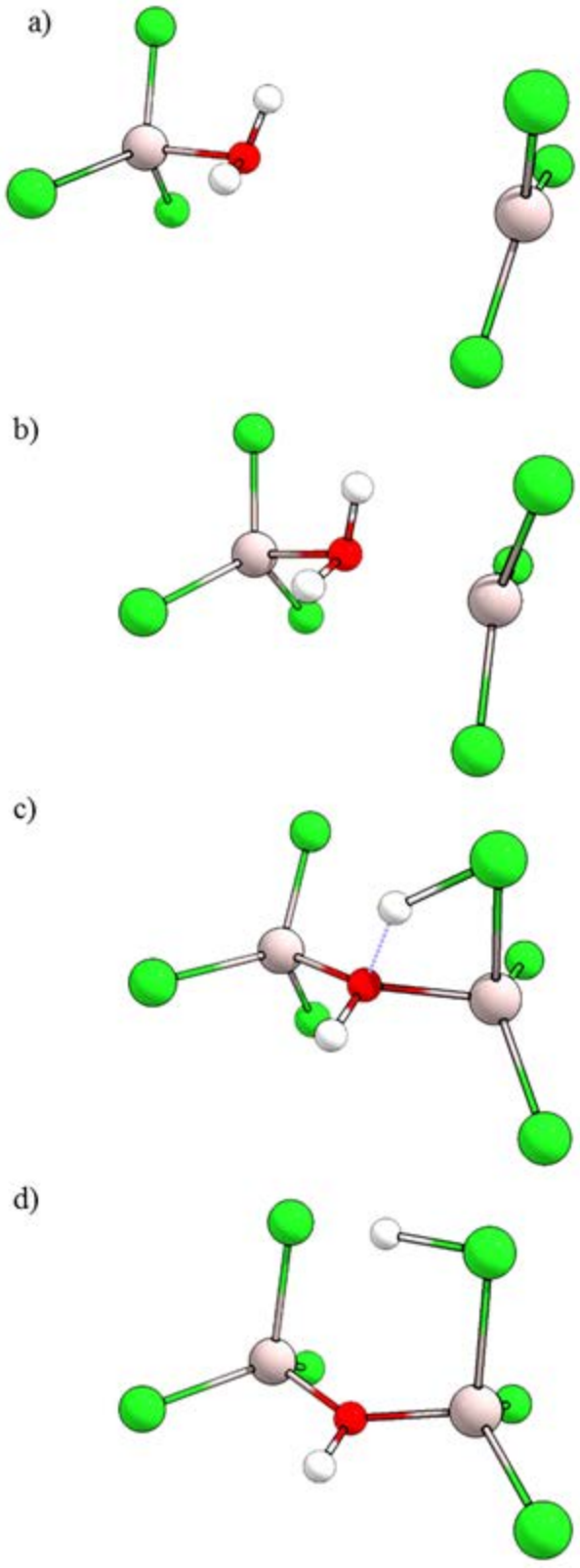

Figure 21. The reaction mechanism for forming the alternate $(AlCl_3)_2H_2O$ complex. a) Initial state b) local minimum state c) transition state and d) product state

The E_a and ΔE_{rxn} values for the formation of this complex are 9.2 kcal/mol and -14.5 kcal/mol, respectively, shown in Figure 22. Again, the reaction barrier is attributed to the proton transfer from the water molecule to a chlorine atom. The final configuration appears to be highly symmetric (C_{2v}), shown in Figure 21d, with the transferred proton positioned in the middle of two chlorine atoms. Even though the formation of this complex has an energy barrier, the E_a value is approximately a third lower in energy than the lowest E_a value calculated for the initiation step with complex II of 14.8 kcal/mol. In this configuration, there are two distinct hydrogens that can be attacked by the IB molecule. We expect the reaction pathway where the IB attacks the proton on the oxygen to be similar to the reaction pathway in Figure 19. Hence, we ran GSM for the reaction the IB attacks the hydrogen coordinated with the chlorine. Key configurations for this reaction are shown in Figure 23.

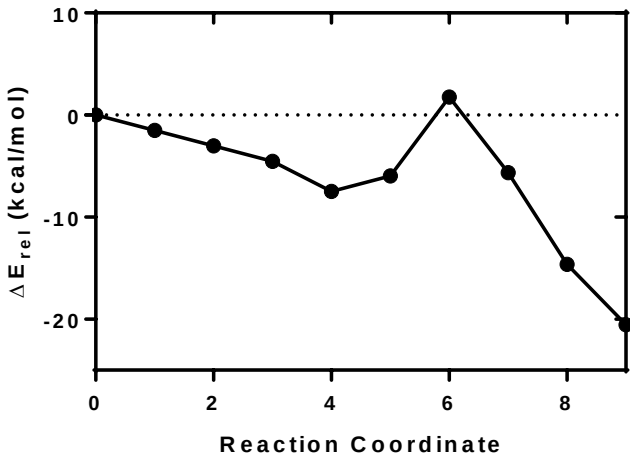

Figure 22. Potential energy surface for the formation of the alternate $(AlCl_3)_2H_2O$ complex calculated at B3LYP/def2-TZVP

The transition state shown in Figure 23 is an early transition where the proton is still bound to the chlorine. The E_a and ΔE_{rxn} for this reaction pathway are 2.4 kcal/mol and -9.2 kcal/mol,

respectively, shown in Figure 24. The activation energy for the proton transfer in this reaction is much lower compared to the barriers calculated previously. This appears to be a promising initiation pathway. The propagation step with this new co-initiator complex is shown in Figure 25.

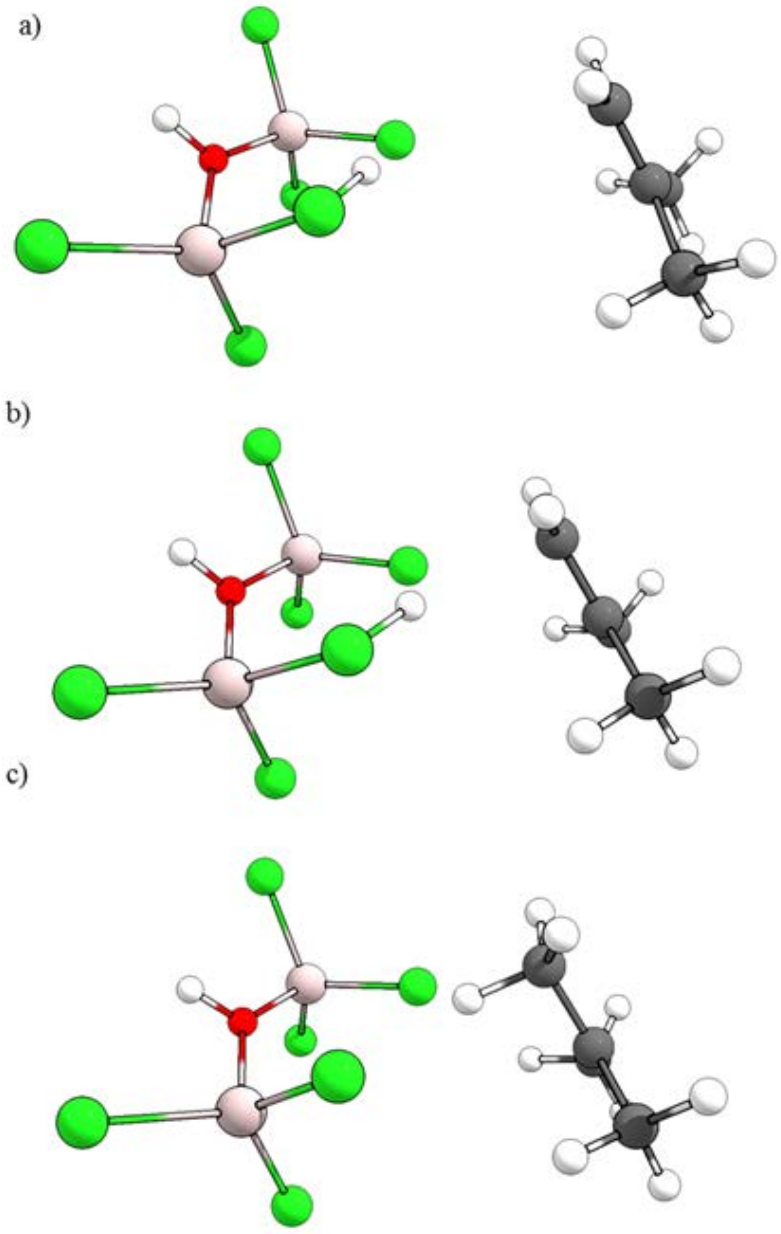

Figure 23. Initiation mechanism with alternate $(AlCl_3)_2H_2O$ complex. a) Local minimum state b) transition state and c) product state

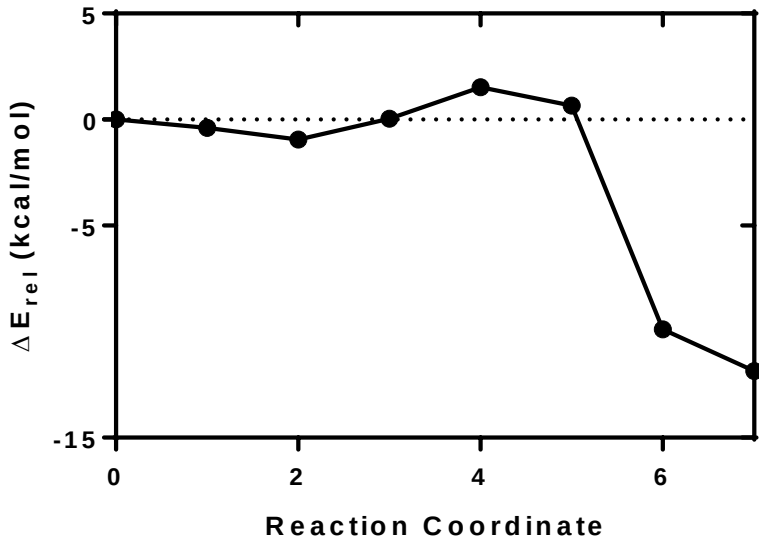

Figure 24. Potential energy surface for the initiation step with alternate $(AlCl_3)_2H_2O$ complex calculated at B3LYP/def2-TZVP

From Figure 25, the second IB molecule is inserted in between the IBH^+ and its negative counterpart. After the IBH^+ forms a bond with the second IB, the two hydrogen atoms on the IBH^+ appears to be weakly coordinated with the chlorine groups. According to Figure 26, the propagation step for the newly identified co-initiator complex has a low activation barrier of 2.9 kcal/mol. This reaction barrier is substantially lower compared to the propagation pathway with complex II and more consistent with the experimental reaction conditions. The ΔE_{rxn} value of -0.69 kcal/mol indicates that the reaction is still exothermic. This could be the potential reaction pathway for cationic polymerization reaction of IB.

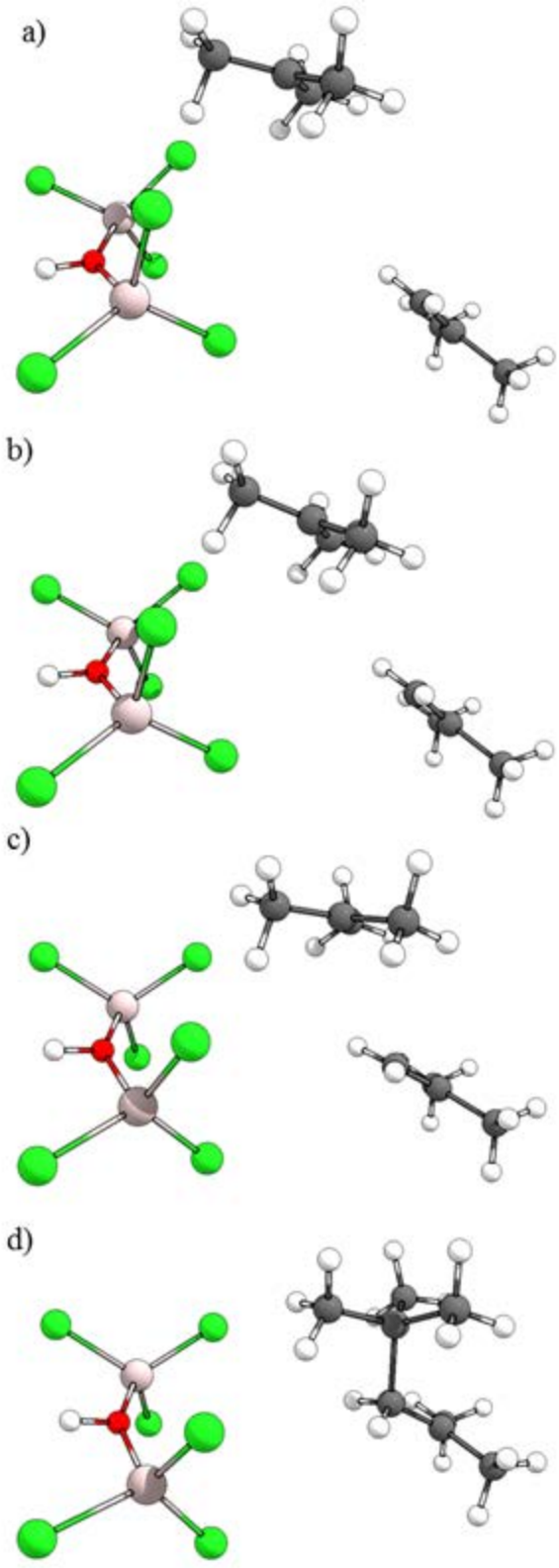

Figure 25. a) Initial configuration, b) transition state, c) local minimum configuration and d) final configuration for alternate the propagation step

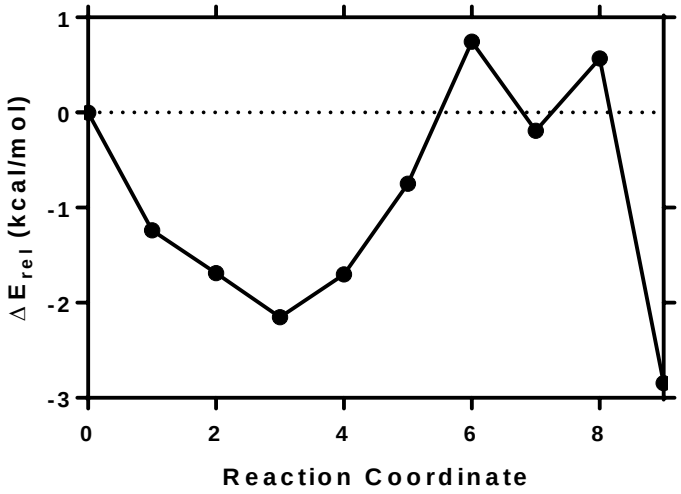

Figure 26. Potential energy surface for the initiation step with alternate $(AlCl_3)_2H_2O$ complex calculated at B3LYP/def2-TZVP

4.4 CONCLUSION

In summary, we found that the formation of $AlCl_3H_2O$, I → II, is thermodynamically favorable and the reaction appears to be barrierless. Although the initiation step, II → V, is thermodynamically favorable, the activation energy is relatively high (E_a = 14.8 kcal/mol for $AlCl_3$ dimer system). The high barrier is attributed to the proton transfer from the water molecule to the IB molecule. Similarly, the propagation step, V → VI, is thermodynamically favorable, but the activation energy is high (E_a = 34.1 kcal/mol). In this case, the high activation barrier is attributed to the breaking of the C-O bond, which was formed in the initiation step.

We found a potential reaction pathway for the initiation step with a low E_a value of 2.4 kcal/mol, but the E_{rxn} value for the formation of the $(AlCl_3)_2H_2O$ complex is 9.2 kcal/mol. The E_a value for the propagation step is 2.9 kcal/mol, which is more consistent with the experimental reaction condition and could be the potential pathway for the polymerization of IBs. Future work

should further study the propagation step, the addition of the third and fourth IB molecules, as well as identify potential termination pathways.

BIBLIOGRAPHY

(1) TANAKA, A.; MAEKAWA, K.; SUZUKI, K. Theoretical Calculations in Reaction Mechanism Studies.

(2) Hafner, J. Ab-initio simulations of materials using VASP: Density-functional theory and beyond. *Journal of computational chemistry* **2008**, *29*, 2044-2078.

(3) Geerlings, P.; De Proft, F.; Langenaeker, W. Conceptual density functional theory. *Chemical reviews* **2003**, *103*, 1793-1874.

(4) Miertuš, S.; Scrocco, E.; Tomasi, J. Electrostatic interaction of a solute with a continuum. A direct utilizaion of AB initio molecular potentials for the prevision of solvent effects. *Chemical Physics* **1981**, *55*, 117-129.

(5) Tomasi, J.; Persico, M. Molecular interactions in solution: an overview of methods based on continuous distributions of the solvent. *Chemical Reviews* **1994**, *94*, 2027-2094.

(6) Cammi, R.; Tomasi, J. Remarks on the use of the apparent surface charges (ASC) methods in solvation problems: Iterative versus matrix-inversion procedures and the renormalization of the apparent charges. *Journal of computational chemistry* **1995**, *16*, 1449-1458.

(7) Klamt, A.; Schuurmann, G. COSMO: a new approach to dielectric screening in solvents with explicit expressions for the screening energy and its gradient. *Journal of the Chemical Society, Perkin Transactions 2* **1993**, 799-805.

(8) Barone, V.; Cossi, M. Quantum calculation of molecular energies and energy gradients in solution by a conductor solvent model. *The Journal of Physical Chemistry A* **1998**, *102*, 1995-2001.

(9) Chipman, D. M. Anion electric field is related to hydration energy. *The Journal of chemical physics* **2003**, *118*, 9937-9942.

(10) Camaioni, D. M.; Dupuis, M.; Bentley, J. Theoretical Characterization of Oxoanion, XO mn-, Solvation. *The Journal of Physical Chemistry A* **2003**, *107*, 5778-5788.

(11) Kelly, C. P.; Cramer, C. J.; Truhlar, D. G. SM6: A density functional theory continuum solvation model for calculating aqueous solvation free energies of neutrals, ions, and solute− water clusters. *Journal of chemical theory and computation* **2005**, *1*, 1133-1152.

(12) Kelly, C. P.; Cramer, C. J.; Truhlar, D. G. Aqueous solvation free energies of ions and ion− water clusters based on an accurate value for the absolute aqueous solvation free energy of the proton. *The Journal of Physical Chemistry B* **2006**, *110*, 16066-16081.

(13) Pliego, J. R.; Riveros, J. M. The cluster− continuum model for the calculation of the solvation free energy of ionic species. *The Journal of Physical Chemistry A* **2001**, *105*, 7241-7247.

(14) Mennucci, B.; Martínez, J. M. How to model solvation of peptides? Insights from a quantum-mechanical and molecular dynamics study of N-methylacetamide. 1. Geometries, infrared, and ultraviolet spectra in water. *The Journal of Physical Chemistry B* **2005**, *109*, 9818-9829.

(15) *2011 Critical materials strategy*, 2011.

(16) Barysz, M.; Ishikawa, Y.: *Relativistic methods for chemists*; Springer Science & Business Media, 2010; Vol. 10.

(17) Marenich, A. V.; Ho, J.; Coote, M. L.; Cramer, C. J.; Truhlar, D. G. Computational electrochemistry: prediction of liquid-phase reduction potentials. *Physical Chemistry Chemical Physics* **2014**, *16*, 15068-15106.

(18) Bryantsev, V. S.; Diallo, M. S.; Goddard Iii, W. A. Calculation of solvation free energies of charged solutes using mixed cluster/continuum models. *The Journal of Physical Chemistry B* **2008**, *112*, 9709-9719.

(19) Bryantsev, V. S.; Diallo, M. S.; Van Duin, A. C.; Goddard III, W. A. Hydration of copper (II): new insights from density functional theory and the COSMO solvation model. *The Journal of Physical Chemistry A* **2008**, *112*, 9104-9112.

(20) Zhang, J.; Dolg, M. Global optimization of clusters of rigid molecules using the artificial bee colony algorithm. *Physical Chemistry Chemical Physics* **2016**, *18*, 3003-3010.

(21) Vanommeslaeghe, K.; Hatcher, E.; Acharya, C.; Kundu, S.; Zhong, S.; Shim, J.; Darian, E.; Guvench, O.; Lopes, P.; Vorobyov, I. CHARMM general force field: A force field for drug-like molecules compatible with the CHARMM all-atom additive biological force fields. *Journal of computational chemistry* **2010**, *31*, 671-690.

(22) Abascal, J. L.; Vega, C. A general purpose model for the condensed phases of water: TIP4P/2005. *The Journal of chemical physics* **2005**, *123*, 234505.

(23) Becke, A. D. Density-functional thermochemistry. III. The role of exact exchange. *The Journal of chemical physics* **1993**, *98*, 5648-5652.

(24) Weigend, F.; Ahlrichs, R. Balanced basis sets of split valence, triple zeta valence and quadruple zeta valence quality for H to Rn: Design and assessment of accuracy. *Physical Chemistry Chemical Physics* **2005**, *7*, 3297-3305.

(25) Izsák, R.; Neese, F. An overlap fitted chain of spheres exchange method. *The Journal of chemical physics* **2011**, *135*, 144105.

(26) Weigend, F.; Häser, M.; Patzelt, H.; Ahlrichs, R. RI-MP2: optimized auxiliary basis sets and demonstration of efficiency. *Chemical physics letters* **1998**, *294*, 143-152.

(27) Grimme, S.; Furche, F.; Ahlrichs, R. An improved method for density functional calculations of the frequency-dependent optical rotation. *Chemical physics letters* **2002**, *361*, 321-328.

(28) Marcus, Y.: *Ion solvation*; Wiley, 1985.

(29) Chaboy, J.; Muñoz-Páez, A.; Merkling, P. J.; Sánchez Marcos, E. The hydration of Cu 2+: Can the Jahn-Teller effect be detected in liquid solution? *The Journal of chemical physics* **2006**, *124*, 064509.

(30) Rodríguez-Santiago, L.; Alí-Torres, J.; Vidossich, P.; Sodupe, M. Coordination properties of a metal chelator clioquinol to Zn 2+ studied by static DFT and ab initio molecular dynamics. *Physical Chemistry Chemical Physics* **2015**, *17*, 13582-13589.

(31) Stewart, J. J. Stewart Computational Chemistry, Colorado Springs, CO, USA, 2012. *See* http://OpenMOPAC. *net* **2013**.

(32) Stewart, J. J. Optimization of parameters for semiempirical methods VI: more modifications to the NDDO approximations and re-optimization of parameters. *Journal of molecular modeling* **2013**, *19*, 1-32.

(33) Ellis, R. J.; Brigham, D. M.; Delmau, L.; Ivanov, A. S.; Williams, N. J.; Vo, M. N.; Reinhart, B.; Moyer, B. A.; Bryantsev, V. S. "Straining" to Separate the Rare Earths: How the Lanthanide Contraction Impacts Chelation by Diglycolamide Ligands. *Inorganic Chemistry* **2016**.

(34) Shannon, R. t. Revised effective ionic radii and systematic studies of interatomic distances in halides and chalcogenides. *Acta crystallographica section A: crystal physics, diffraction, theoretical and general crystallography* **1976**, *32*, 751-767.

(35) Xie, F.; Zhang, T. A.; Dreisinger, D.; Doyle, F. A critical review on solvent extraction of rare earths from aqueous solutions. *Minerals Engineering* **2014**, *56*, 10-28.

(36) Wilson, A. M.; Bailey, P. J.; Tasker, P. A.; Turkington, J. R.; Grant, R. A.; Love, J. B. Solvent extraction: the coordination chemistry behind extractive metallurgy. *Chemical Society Reviews* **2014**, *43*, 123-134.

(37) Regueiro-Figueroa, M.; Esteban-Gómez, D.; de Blas, A.; Rodríguez-Blas, T.; Platas-Iglesias, C. Understanding stability trends along the lanthanide series. *Chemistry–A European Journal* **2014**, *20*, 3974-3981.

(38) Hancock, R. D.; Bartolotti, L. J. A DFT study of the affinity of lanthanide and actinide ions for sulfur-donor and nitrogen-donor ligands in aqueous solution. *Inorganica Chimica Acta* **2013**, *396*, 101-107.

(39) Ivanov, A. S.; Bryantsev, V. S. A Computational Approach to Predicting Ligand Selectivity for the Size-Based Separation of Trivalent Lanthanides. *European Journal of Inorganic Chemistry* **2016**, *2016*, 3474-3479.

(40) Frisch, M.; Trucks, G.; Schlegel, H.; Scuseria, G.; Robb, M.; Cheeseman, J.; Scalmani, G.; Barone, V.; Mennucci, B.; Petersson, G.: Gaussian 09, revision D. 01. Gaussian, Inc., Wallingford CT, 2009.

(41) Dolg, M.; Stoll, H.; Preuss, H. Energy-adjusted abinitio pseudopotentials for the rare earth elements. *The Journal of Chemical Physics* **1989**, *90*, 1730-1734.

(42) Ribeiro, R. F.; Marenich, A. V.; Cramer, C. J.; Truhlar, D. G. Use of solution-phase vibrational frequencies in continuum models for the free energy of solvation. *The Journal of Physical Chemistry B* **2011**, *115*, 14556-14562.

(43) Tomasi, J.; Mennucci, B.; Cammi, R. Quantum mechanical continuum solvation models. *Chemical reviews* **2005**, *105*, 2999-3094.

(44) Zheng, J.; Xu, X.; Truhlar, D. G. Minimally augmented Karlsruhe basis sets. *Theoretical Chemistry Accounts* **2011**, *128*, 295-305.

(45) Zhao, Y.; Truhlar, D. G. A new local density functional for main-group thermochemistry, transition metal bonding, thermochemical kinetics, and noncovalent interactions. *The Journal of chemical physics* **2006**, *125*, 194101.

(46) Chai, J.-D.; Head-Gordon, M. Long-range corrected hybrid density functionals with damped atom–atom dispersion corrections. *Physical Chemistry Chemical Physics* **2008**, *10*, 6615-6620.

(47) Neese, F. The ORCA program system. *Wiley Interdisciplinary Reviews: Computational Molecular Science* **2012**, *2*, 73-78.

(48) Van Lenthe, E.; Snijders, J.; Baerends, E. The zero-order regular approximation for relativistic effects: The effect of spin–orbit coupling in closed shell molecules. *The Journal of chemical physics* **1996**, *105*, 6505-6516.

(49) Vukovic, S.; Hay, B. P.; Bryantsev, V. S. Predicting Stability Constants for Uranyl Complexes Using Density Functional Theory. *Inorganic chemistry* **2015**, *54*, 3995-4001.

(50) Sasaki, Y.; Tsubata, Y.; Kitatsuji, Y.; Sugo, Y.; Shirasu, N.; Morita, Y.; Kimura, T. Extraction behavior of metal ions by TODGA, DOODA, MIDOA, and NTAamide extractants from HNO3 to n-Dodecane. *Solvent Extraction and Ion Exchange* **2013**, *31*, 401-415.

(51) Sasaki, Y.; Tachimori, S. Extraction of actinides (III),(IV),(V),(VI), and lanthanides (III) by structurally tailored diamides. *Solvent Extraction and Ion Exchange* **2002**, *20*, 21-34.

(52) Sasaki, Y.; Kitatsuji, Y.; Yumi, S.; Tsubata, Y.; Kimura, T.; Morita, Y. Actinides extractability trends for multidentate diamides and phosphine oxides. *Solvent Extraction Research and Development, Japan* **2012**, *19*, 51-61.

(53) Turanov, A.; Karandashev, V.; Baulin, V. Extraction of rare-earth elements from nitric solutions by phosphoryl-containing podands. *Solvent extraction and ion exchange* **1999**, *17*, 1423-1444.

(54) Turanov, A.; Karandashev, V.; Baulin, V.; Yarkevich, A.; Safronova, Z. Extraction of Lanthanides (III) from Aqueous Nitrate Media with Tetra-(p-tolyl)[(o-Phenylene) Oxymethylene] Diphosphine Dioxide. *Solvent Extraction and Ion Exchange* **2009**, *27*, 551-578.

(55) Odian, G.: *Principles of Polymerization*; 4th ed.; John Wiley & Son, Inc: Hoboken, New Jersey, 2004.

(56) Vasilenko, I. V.; Frolov, A. N.; Kostjuk, S. V. Cationic Polymerization of Isobutylene Using AlCl3OBu2as a Coinitiator: Synthesis of Highly Reactive Polyisobutylene. *Macromolecules* **2010**, *43*, 5503-5507.

(57) Kennedy, J. P.; Rengachary, S.: Correlation between cationic model and polymerization reactions of olefins. In *Fortschritte der Hochpolymeren-Forschung*; Springer, 1974; pp 1-48.

(58) Evans, A. G.; Meadows, G. W. The polymerization of isobutene by boron trifluoride. *Transactions of the Faraday Society* **1950**, *46*, 327-331.

(59) Evans, A. G.; Meadows, G. The polymerization of iso butene by boron trifluoride. *Transactions of the Faraday Society* **1950**, *46*, 327-331.

(60) Kostjuk, S. V.; Yeong, H. Y.; Voit, B. Cationic polymerization of isobutylene at room temperature. *Journal of Polymer Science Part A: Polymer Chemistry* **2013**, *51*, 471-486.

(61) Perdew, J. P. Density-functional approximation for the correlation energy of the inhomogeneous electron gas. *Physical Review B* **1986**, *33*, 8822.

(62) Zimmerman, P. M. Single-ended transition state finding with the growing string method. *Journal of computational chemistry* **2015**, *36*, 601-611.

(63) Zimmerman, P. Reliable transition state searches integrated with the growing string method. *Journal of Chemical Theory and Computation* **2013**, *9*, 3043-3050.

(64) Dunn, D. J.: 'The Cationic Polymerization of Vinyl Monomers. In *Developments in polymerization*; Appl. Sci. Publishers London, 1979; Vol. 1.